6-19-2014

Proton Damage Effects on Carbon Nanotube Field-Effect Transistors

Evan R. Kemp

PROTON DAMAGE EFFECTS ON CARBON NANOTUBE FIELD-EFFECT TRANSISTORS

THESIS

Evan R. Kemp, Ctr, USAF

AFIT-ENP-T-14-J-39

DEPARTMENT OF THE AIR FORCE
AIR UNIVERSITY

AIR FORCE INSTITUTE OF TECHNOLOGY

Wright-Patterson Air Force Base, Ohio

AFIT-ENP-T-14-J-39

PROTON DAMAGE EFFECTS ON CARBON NANOTUBE FIELD-EFFECT TRANSISTORS

THESIS

Presented to the Faculty
Department of Engineering Physics
Graduate School of Engineering and Management
Air Force Institute of Technology
Air University
Air Education and Training Command
in Partial Fulfillment of the Requirements for the
Degree of Master of Science in Material Science

Evan R. Kemp, BS
Ctr, USAF

June 2014

AFIT-ENP-T-14-J-39

PROTON DAMAGE EFFECTS ON CARBON NANOTUBE FIELD-EFFECT TRANSISTORS

Evan R. Kemp, BS
Ctr, USAF

Approved:

// Signed //_____	__28 May 2014__
John W. McClory, PhD (Chairman)	Date
// Signed //_____	__27 May 2014__
Major Timothy W. Zens, PhD (Member)	Date
// Signed //_____	__27 May 2014__
James C. Petrosky, PhD (Member)	Date
// Signed //_____	__27 May 2014__
Sarah A. Francis, PhD (Member)	Date

AFIT-ENP-T-14-J-39

Abstract

This research investigated the effects of proton damage on single-walled carbon nanotube (SWCNT) transistors. The transistors were irradiated by 1.8 MeV protons to determine the damage induced in the SWCNTs and the device substrate using Raman spectroscopy, and to observe the effect on transistor functionality by measuring current-voltage characteristics. Irradiation of the SWCNT transistors to a fluence of 1×10^{13} protons/cm^2 resulted in 67% increase in the Raman *D/G* peak intensity ratio, while at a fluence of 2×10^{13} protons/cm^2 the increase in the *D/G* ratio was only 18%, likely due to radiation annealing. Current-voltage measurements indicated an increasingly negative threshold voltage shift in SWCNT transistors as a function of proton fluence: -1.3 V after a fluence of 1×10^{12} protons/cm^{2}and -1.9 V after a fluence of 2×10^{13} protons/cm^2. The drain current decreased 33% after a fluence of 1×10^{12} protons/cm^2 and 58% after a fluence of 2×10^{13} protons/cm^2. Charge pumping of the SWCNT transistors revealed a significant error attributed to the combination of the non-uniform distribution of SWCNTs across the gate region, adsorbates on the exposed SWCNT and gate oxide surfaces, and inconsistency in transistor performance. The transistor hysteresis also increased as a function of the proton fluence due to interface and bulk charge trapping. This research provided insight into the effect on SWCNT transistors due to proton irradiations up to a fluence of 2×10^{13} protons/cm^2 demonstrating both interface and bulk damage effects.

Table of Contents

Page

Abstract iv

Table of Contents v

List of Figures viii

List of Tables xiii

I. Introduction 1

1.1 Objectives 3

1.2 Overview of Research 4

1.3 Impacts 5

II. Background 6

2.1 Metal-Oxide-Semiconductor Field-Effect Transistor 6

2.1.1 Theory 6

2.1.2 Charge Pumping 7

2.2 Carbon Nanotubes 10

2.2.1 Synthesis 11

2.2.2 Semiconducting vs. Metallic Nanotubes 12

2.2.3 Raman Spectroscopy 15

2.2.4 Annealing 17

2.3 Carbon Nanotube Transistors 18

2.3.1 Theory 18

2.3.2 Design/Structure 19
2.3.3 Hysteresis 21
2.4 Radiation Effects 22
2.4.1 Proton Damage Effects 22
2.4.2 Silicon Damage 23
2.4.3 SWCNT Damage 26
2.4.4 Previous Research – SWCNT FET 29

III. Experiment 32
3.1 Purpose 32
3.2 Experiment Setup and Design 32
3.2.1 Transistors 32
3.2.2 Current-Voltage Characteristics 35
3.2.3 Charge Pumping 39
3.2.4 Raman Spectroscopy 42
3.2.5 Proton Irradiation 44

IV. Results and Analysis 47
4.1 Raman Study 47
4.1.1 Semiconducting SWCNT Transistors 47
4.1.2 Semiconducting/Metallic SWCNT Transistors 50
4.2 Charge Pumping Study 53
4.2.1 Semiconducting SWCNT Transistors 53
4.2.2 Semiconducting/Metallic SWCNT transistors 56
4.3 Current-Voltage Characterization Study 59
4.3.1 Semiconducting SWCNT Transistors 60
4.3.2 Semiconducting/Metallic Transistors 67

V. Conclusions 70
5.1 Raman Study 70

5.2 Charge Pumping Study 70
5.3 Current-Voltage Characterization 71
5.4 Future Work 72
5.5 Overall Conclusions 73

Bibliography 75

List of Figures

Figure Page

1. Depiction of the proton energy spectra in low Earth orbit for both the solar minimum and maximum. The proton energy spectra is presented in terms of the average daily proton flux. Reproduced with permission from Stassinopoulus *et al*. [11]. 2

2. Illustration depicting the cross section of a simplified n-channel silicon MOSFET. 6

3. Wire diagram of carbon atoms depicting the rolled graphitic cylinder of sp^2-bonded carbon atoms. Reproduced with permission from Best [10]..... 10

4. Illustration depicting the separation of CNTs by ultra-centrifugation. The optical contrast between layers observed is due to the correlation between the diameter of the CNTs and the magnitude of their band gap. Reproduced with permission from Arnold *et al*. [27]. 13

5. Planar wire diagram of sp^2-oriented carbon atoms or a sheet of graphene depicting the three major chiral vectors that separate the electronic properties observed in SWCNTs. The chiral vectors depicted are the vectors a sheet of graphene sheet would be rolled about to form a SWCNT. Reproduced with permission from Best [10]. 14

6. Raman spectra from metallic and semiconducting SWCNTs using a 785 nm laser, showing the key vibrational modes observable for SWCNTs. Illustrations depict the RBM and *G*-band, with arrows showing the directions of atom movement in each mode. '*' denote vibrational modes of silicon, the substrate used. Reproduced with permission from Dresselhaus *et al*. [31]..... 16

7. Illustration depicting defects (right) and defect annealing (left) in SWCNTs. During annealing the double vacancy (D), single vacancy (S) and the interstitial carbon atom (A) rearrange due to thermal excitation to reach a more stable bonding state with the reformation of the carbon network. Reproduced with permission from Krasheninnikov *et al*. [36]. 17

Figure Page

8. (a) Illustration of the band diagram with the Schottky barrier difference for different nanotube diameters, using the same metal at both contacts. (b) Illustration the Schottky barrier difference using different metals at each contact with a uniform carbon nanotube diameter. Reproduced with permission from Chen *et al*. [37]. 18

9. Illustration depicting the dynamic screening effect of injected charges. Holes or electrons are injected into traps based on the gate bias applied. Reproduced with permission from Ong *et al*. [43]. 21

10. Illustration relating the energy of incident protons into a silicon-based material to the frequency and extent of the knock on effects categorized as free defects, single cascades and many cascades. Reproduced with permission from Srour *et al*. [49].....24

11. Fraction of uncombined holes as a function of the applied electric field for gamma rays, x-rays, low-energy protons and alpha particles. Reproduced with permission from Schwank *et al*. [50].....26

12. Temperature-dependent conductivity measurements as a function of alpha fluence on SWCNT film samples showing a decrease in the conductivity with increasing radiation fluences. Reproduced with permission from Cress *et al*. [8]. 28

13. Raman spectra for both SWCNT and MWCNT thin films as a function of the increasing ion fluences for 150 keV boron ions. Reproduced with permission from Rossi *et al*. [6].....28

14. Raman spectra presented before and after irradiation (top), along with the *D/G* ratio as a function of channel width (bottom). Reproduced with permission from Francis *et al*. [3].....30

15. Interface trap density as a function of distance from the SWCNT/gate oxide interface before and after irradiation and annealing. Reproduced with permission from Francis *et al*. [3].....31

16. Drain current and gate current magnitude as a function of the applied gate voltage before and after electron irradiation. Reproduced with permission from Francis *et al*. [3]. 31

Figure Page

17. Diagram representing a cross section of the back-gated CNTFET design. 33

18. The semiconducting SWCNT chip depicting the total number of reticles fabricated on a single chip. Only the center reticles contained devices due to the SWCNT film size.....34

19. A single transistor reticle with the 10× objective of an optical microscope, depicting the 36 unique transistor devices present in each reticle. The channel length and width differences can be observed clearly. 35

20. The Signatone probe station used to test individual transistors for both current-voltage characterization and charge pumping measurements. The Keithley 4200-SCS and Agilent 33220A connect directly to the probes via coaxial cables. 36

21. Representative *I-V* curve of a semiconducting SWCNT transistor on a linear plot. 37

22. Drain current as a function of gate voltage for the semiconducting SWCNT transistor EKS01, before and after irradiation, illustrating the method used to determine the threshold voltage shift. 38

23. Drain current as a function of gate voltage for the semiconducting SWCNT transistor EKS01, before and after irradiation, illustrating the reduction in drain current and hysteresis. 38

24. Experimental setup for charge pumping measurements. A positive bias is placed on the drain, where the current is measured as the charge pumping current I_{CP}. The gate is pulsed between inversion and accumulation using a function generator. 41

25. Charge pumped per cycle, Q_{CP}, as a function of frequency for a semiconducting CNT transistor using a peak-to-peak voltage, V_{PP}, of 2 V. Gate area dimensions are 2 μm long by 128 μm wide. 41

26. Representative Raman spectrum for the semiconducting SWCNT transistor EKS01 prior to irradiation.....43

27. Representative Raman measurement for the semiconducting/metallic SWCNT transistor EKSM01 prior to irradiation. 43

Figure Page

28. The arrangement of sample reticles, along with several ride-along samples for other projects mounted on the steel back plate that was used as a charge sink during irradiations, and to fix the samples in the beam line. 45

29. Vertically mounted samples in the sample chamber, with several ride-along samples. The sample mount is aligned with the beam line and the dosimetry equipment can be seen attached to the sample stage. The arrow shows the direction of the beam line 46

30. The sample mounting stage showing the horizontal orientation of the stage required for vertical sample mounting. 46

31. Normalized Raman spectra for EKS01, the semiconducting SWCNT transistor sample, before and after irradiation to fluences of 10^{12}, 10^{13}, and 2×10^{13} protons/cm^2. Spectra are normalized to the magnitude of the *G* peak. The *D* peak is barely observable above the noise and background of the Raman measurement. 48

32. The measured *D* peak for the semiconducting sample, before and after irradiation to fluences of 10^{12}, 10^{13}, and 2×10^{13} protons/cm^2. Spectra shows the significant amount of noise observed due to the low density of SWCNTs across the gate area. The spectra show that the intensity of the *D* peak does not increase or change significantly as a function of proton flux for this low density dispersion of SWCNTs across the gate. 49

33. Normalized Raman spectra for EKSM01, the semiconducting/metallic SWCNT transistor sample, before and after irradiation to fluences of 10^{12}, 10^{13}, and 2×10^{13} protons/cm^2. Spectra are normalized to the magnitude of the *G* peak. 52

34. Raman spectra specifically showing the *D* peak observed in EKSM01 as a function of proton fluence. An increase is observed due to proton irradiation; however, a clear trend as a function of the fluence is not observed. 52

35. Interface trap density as a function of distance from the interface for EKS01 semiconducting SWCNT transistors, before and after irradiation to fluences of 10^{12}, 10^{13}, and 2×10^{13} protons/cm^2, plotted on a linear scale to highlight the error in the interface trap density calculated across all transistors on each reticle. The same interface trap profile is seen across all transistors, however no trend with proton fluence is observed. 55

Figure Page

36. Interface trap density as a function of distance from the interface for EKS01 semiconducting SWCNT transistors, before and after irradiation to fluences of 10^{12}, 10^{13}, and 2×10^{13} protons/cm^2, plotted on a semi-log scale. A similar trend of trap densities is observed across all transistors. Calculated trap density is reduced post-irradiation relative to pre-irradiation. 55

37. Interface trap density as a function of distance from the interface for the EKSM01 semiconducting/metallic SWCNT transistors, before and after irradiation to fluences of 10^{12}, 10^{13}, and 2×10^{13} protons/cm^2, plotted on a linear scale to highlight the error in the interface trap densities calculated across all transistors on each reticle. 58

38. Interface trap density as a function of distance from the interface for the EKSM01 semiconducting/metallic SWCNT transistors, before and after irradiation to fluences of 10^{12}, 10^{13}, and 2×10^{13} protons/cm^2, plotted on a semi-log scale. 58

39. Drain current as a function of gate voltage for semiconducting/metallic SWCNT transistors EKSM01 before and after irradiation to a fluence of 2×10^{13} protons/cm^2. Drain current shows the poor on/off characteristics with a hysteresis of 0.1 V before proton irradiation and 0.5 V after. 59

40. Diagram depicting the location of charge deposition in the gate oxide due to continuous proton irradiation. 61

41. Threshold voltage shift as a function of proton fluence illustrating the increasing negative shift in the threshold voltage with increasing proton fluence for EKS01 semiconducting SWCNT transistors following proton irradiation. 62

42. The average gate leakage current across all reticles of EKS01 at each proton fluence as a function of the gate voltage. There is no observable increase in the gate leakage current due to increasing proton fluence, instead a uniform decrease is observed at all proton fluences. 66

43. The average gate leakage current across all reticles of EKSM01 before and after proton irradiation. There is no observable increase in the gate leakage current due to increasing proton fluence. The gate current decreases slightly with the increasing proton fluence. 69

List of Tables

Table Page

1. The *D/G* ratios for EKS01, the semiconducting SWCNT transistor sample, before and after proton irradiation. The fluences are presented, with all irradiations performed using 1.8 MeV protons. 49

2. The *D/G* ratios for EKSM01, the semiconducting/metallic SWCNT transistor sample, before and after proton irradiation. The fluences are presented with all irradiations performed using 1.8 MeV protons. Values show an increase in the *D/G* ratio due to radiation, however the apparent trend increases up to 1×10^{13} protons. However, the same trend does not continue for irradiations up to 2×10^{13} protons/cm^2 51

3. Interface trap density for EKS01 semiconducting transistor reticles before and after proton irradiation to fluences 1×10^{12}, 1×10^{13}, and 2×10^{13} protons/cm^2. 56

4. Interface trap density for EKSM01 semiconducting/metallic transistor reticles before and after proton irradiation to fluences of 1×10^{12}, 1×10^{13}, and 2×10^{13} protons/cm^2. An apparent increase of interface traps at 1.09 nm as a function of fluence is observed. 57

5. The threshold voltage shift in EKS01 semiconducting SWCNT transistors following irradiation to fluences of 1×10^{12}, 1×10^{13}, and 2×10^{13} protons/cm^2. While the standard deviation is significant, an apparent trend can be observed as the threshold voltage shift increases with increasing proton fluence. 61

6. Table of the calculated downshift, or reduction in drain current relative to the initial drain current at the 50% level of the on/off point, before and after proton irradiation. Values show an increasing downshift with increasing proton fluence, which correlates to an increasing reduction in drain current. Presented values are an average across all transistors on a single reticle. 64

7. The relative change in the measured transistor hysteresis for EKS01 semiconducting SWCNT transistors before and after proton irradiation. The hysteresis is presented at three selected states to show the variability across each transistor and the instability of transistor properties near the on and off state. 65

Table Page

8. The average gate leakage current at each proton fluence along with the change in current relative to the pre-irradiation measurements for EKS01 semiconducting SWCNT transistors following 1.8 MeV proton irradiation. The standard deviation is presented as a measure of the device to device consistency in the gate leakage current. A nearly constant relative decrease can be observed. 66

9. The measured downshift, or reduction in drain current relative to the initial drain current, before and after proton irradiation. A downshift is observed due to proton irradiation, however as the values make it apparent there is no function of fluence observed. 67

10. The relative change in the measured transistor hysteresis before and after irradiation for the EKSM01 semiconducting/metallic SWCNT transistors. The hysteresis is measured at the 50% level of the on/off state for all transistors. An increase in the relative change is observed as a function of the proton fluence. 68

11. The average gate leakage current at each proton fluence along with the change relative to the pre-irradiation measurements for EKSM01 semiconducting/metallic SWCNT transistors. The standard deviation is presented as a measure of the device to device consistency of the gate leakage current. No trend in the relative decrease in gate leakage current is observed with increasing proton fluence. 69

PROTON DAMAGE EFFECTS ON CARBON NANOTUBE FIELD-EFFECT TRANSISTORS

I. Introduction

Originally discovered in 1991 by Sumio Iijima [1], carbon nanotubes (CNTs) have become a highlight of recent electronics research and development, encompassing a large variety of applications due to their unique electrical, thermal, and physical properties. In comparison to commonly utilized materials, CNTs have one hundred times the tensile strength of steel, a thermal conductivity higher than all but pure diamond and an electrical conductivity comparable to copper [2].

The electrical properties of carbon nanotubes are unique. The chirality of the carbon atoms in a CNT alter the conduction mechanisms such that CNTs can be either metallic or semiconducting. Semiconducting CNTs are potentially useful in applications such as transistors to replace silicon-based devices, which are increasingly difficult to fabricate as transistors continually decrease in size. Theoretically CNT-based transistors could exceed the current size limit of silicon-based transistors (22nm gate widths), increasing the number of transistors per area with reduced heat buildup due to their excellent thermal properties. Research has shown that carbon nanotubes are also more resistant to radiation than modern silicon-based devices [3-11].

The most common environment and application requiring the need for radiation-resistant electronics involves space and satellite applications. This radiation environment

includes a broad spectrum of electron, proton and ion energies ranging from keV to 10's of MeV. Proton energies in the 1.8 MeV range are experienced in the mid-energy range of the proton energy spectrum in low Earth orbit, as shown in Figure 1, reproduced from Stassinopoulus *et al.* [11].

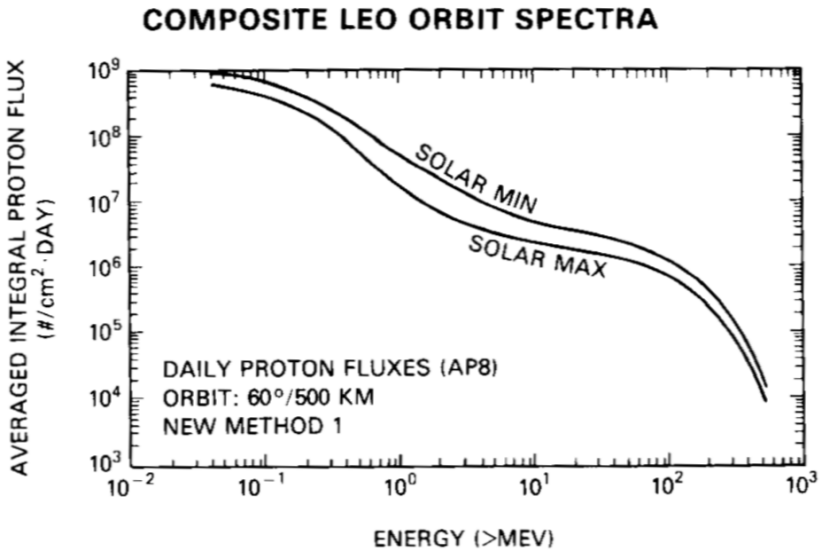

Figure 1: Depiction of the proton energy spectra in low Earth orbit for both the solar minimum and maximum. The proton energy spectra is presented in terms of the average daily proton flux. Reproduced with permission from Stassinopoulus *et al.* [11].

The 1.8 MeV proton flux observed is between 2.5 to 5×10^6 protons/cm^2 per day between solar maximum and solar minimum. Taking a nominal value of 3.5×10^6 protons/cm^2 per day, the yearly proton fluence observed in the low Earth orbit is approximately 1.3×10^9 protons/ cm^2 at an energy of 1.8 MeV. With a large variety of satellite lifetimes ranging from 5 years to a record setting 50 years, the components in a satellite could experience a proton fluence of 1.8 MeV protons from 6.4×10^9 to 6.4×10^{10} protons/cm^2. However based on previous research, total proton fluences exceeding 10^{12} protons/cm^2 are required to observe significant radiation damage effects.

1.1 Objectives

The objective of this research is to understand the physical and electrical changes to single-wall carbon nanotube transistors (SWCNT) due to exposure in a proton radiation environment. Following ion, electron and high-energy proton irradiations on SWCNT transistors by Francis *et al.* [3] and Hong *et al.* [4] and SWCNT films by Best [10], this work seeks to analyze proton irradiation damage effects in SWCNT transistors in order to correlate with the data and calculations in previous research. The total fluence was chosen based on the total displacement damage dose (DDD), which was based on the non-ionizing energy loss (NIEL) damage of 1 MeV electrons in silicon compared to that of 1.8 MeV protons in silicon. The ratio of the NIEL damage is 10^{-4} [12], resulting in the lower bound of the 1×10^{12} protons/cm^2 fluence investigated, in comparison to a fluence of 1×10^{16} electrons/cm^2 [3]. Specifically, this study seeks to correlate the current-voltage characterization, changes to the Raman spectra, and the results of charge pumping to the results of these previous studies, as well as to determine the effects of varying proton fluences. Proton irradiations were carried out at the Institute of Space Defense and Electronics (ISDE) Pelletron accelerator facility at Vanderbilt University. Measurements were taken pre- and post-irradiation to analyze and understand the radiation effects on these devices. Further analysis using Raman spectroscopy enabled an investigation of the radiation effects on the SWCNTs, as well as an understanding of the effects on device properties. Charge pumping provided further insight into the radiation damage due to trapping at all interfaces surrounding the SWCNTs and the substrate. In the future, these

transistors can be improved in terms of device performance and radiation hardness for use as field-effect transistors for space applications.

1.2 Overview of Research

This research consists of SWCNT back-gated field-effect transistors irradiated with 1.8 MeV protons to fluences ranging from 10^{12} to 10^{13} protons/cm^2, in order to observe and quantify changes to the transistor functionality and the changes in the electrical properties of the materials (SWCNTs and SiO_2) that constitute the devices. These changes may be caused by structural damage such as carbon atom displacement causing defects in the carbon nanotubes as well as by trap formation and charging in the silicon dioxide. Similar research has been conducted using electrons [3], [9] and higher energy protons on SWCNT back-gated transistors [4]. Electrical characterization includes pre- and post-irradiation current-voltage measurements for the purpose of observing changes in drain current, shifts in the threshold voltage, and changes to transistor hysteresis as a function of proton fluence. In addition to the current-voltage characterization, samples are measured using a charge pumping method modified from the standard method used on traditional metal oxide semiconductor (MOS) structures to determine the interface trap density at the SWCNT/SiO_2 interface pre- and post-irradiation. Pre- and post-irradiation Raman spectroscopy measurements are used to assess radiation damage to the SWCNTs by observing any changes to the *D* and *G* peaks as a function of proton fluence. All studies are completed at ambient temperature and humidity.

1.3 Impacts

Previous research by Cress *et al.* on SWCNT thin films showed the expected decrease in conductivity due to non-ionizing radiation should be minimal based on the displacement damage dose for 1.8 MeV proton fluences in this study, as demonstrated in his investigation of alpha irradiation, in comparison to literature on carbon ions and 2 MeV protons [8]. This change in resistivity was measured in other studies and found to be a function of radiation fluence using Raman spectroscopic measurements. However, studies based on ionizing damage show a significant decrease in the drain current [3], [9], via measurement of current-voltage characteristics and charge pumping current.

In this research, minimal displacement damage to the SWCNTs due to knock-on effects was observed. This was confirmed by analyzing the changes in the Raman spectra as a function of proton fluence, which manifested itself as a minimal increase in the ratio of the intensity of the *D* peak relative to the intensity of the *G* peak. A significant increase in the *D* peak would correlate to significant CNT damage; however, this was not observed. The interface trap density did not increase as a function of proton fluence, which is in contrast to what is typically observed in irradiated MOS devices [12]; a negative shift in the threshold voltage was also observed.

II. Background

2.1 Metal-Oxide-Semiconductor Field-Effect Transistor

2.1.1 Theory

Silicon-based metal-oxide-semiconductor field-effect transistors (MOSFETs) are the basis for today's transistors and computers. An illustration of a top-gated MOSFET cross section is shown in Figure 2. In the case of an n-channel MOSFET, a p-type silicon substrate is doped at the source and drain with excess dopants to make it n-type. The distance between the source and drain is considered the channel length, and the gate area covers the entire channel region. In the majority of devices, silicon dioxide (SiO_2) is used as the gate dielectric.

Figure 2: Illustration depicting the cross section of a simplified n-channel silicon MOSFET.

The MOSFET functions as a switch, so that when the voltage applied to the gate overcomes the device threshold voltage, and a small reverse bias is applied to either the source or drain, current can flow between the source and drain contacts. Current flows

after charge accumulates at the surface of the gate dielectric. In the case of an n-channel device, the p-type substrate beneath the gate oxide becomes saturated with the minority carrier (electrons) when a positive voltage is applied to the gate, drawing negative charge to the interface. In a way, the silicon at the interface becomes more n-like, creating a conduction channel between the source and the drain [13], [14].

2.1.2 Charge Pumping

Interface traps exist at the interfaces in semiconductor devices due to the lattice mismatch between different materials. Interface traps function as charge trapping centers, and are an important measurement of the interface quality. Since radiation can change the quality of the interface through direct damage or by making carriers available to become trapped at the interface, characterization of the interface is important for assessing radiation response.

Charge pumping is a technique that is commonly used to measure interface trap densities in MOS devices. By applying a voltage pulse on the gate such that the device is switched between accumulation and inversion, a recombination current is generated from holes and electrons that are alternately brought to the surface and recombine at trap sites [15]. This measured recombination current is directly proportional to the interface trap density. By varying the frequency of the pulse, a trap density as a function of depth from the interface can be determined [15], [16].

A dependence on the shape of the pulse can be observed when comparing triangle and square waves, seen as a non-linear dependence of the recombination current as a function of frequency. This is observed because the frequency dependence of the rise and fall times gives rise to a frequency dependence of the emitted charge, and therefore a

frequency dependence of the charge recombining with the substrate majority carriers [15].

The variable frequency technique enables the determination of the spatial distribution of the traps at the interface. The interface trap profile in both directions from the interface can be estimated as [3], [16]:

$$D_{it}(z) = -\frac{1}{q\lambda A_G \Delta E}\frac{dQ_{CP}}{dln(f)}, \tag{1}$$

where q is the electron charge, λ is the tunnel attenuation coefficient at the SiO_2 interface, A_G is the gate area, $Q_{CP} = I_{CP}/f$ is the charge recombined per cycle, f is the pulse frequency, z is the distance from the interface, and ΔE is the energy range swept between the high and low gate voltage, and can be estimated by [3], [15], [17]:

$$\Delta E = E - E_i = \pm kTln\left[v_{th}\sigma_{\frac{p}{n}} n_i \frac{|V_{fb} - V_T|}{|\Delta V_G|} t_{\frac{r}{f}}\right]. \tag{2}$$

In (2), k is the Boltzmann constant, T is the temperature, v_{th} is the carrier thermal velocity, $\sigma_{p/n}$ is the carrier capture cross section, n_i is the free carrier concentration, V_{fb} is the flat band voltage, and is estimated at the gate voltage where $I_{CP} = I_{Cpmax}/2$, V_T is the threshold voltage, $\Delta V_G = V_{GH} - V_{GL}$, and $t_{r/f}$ is the rise/fall time of the pulse. The carrier thermal velocity is calculated using the effective mass [3], [18]:

$$m^* = \frac{2\hbar}{3dv_0}, \tag{3}$$

where ħ is the reduced Planck constant, d is the average diameter of the nanotube and v_0 is the Fermi velocity. The tunnel attenuation coefficient is calculated using [3], [16]:

$$\lambda = \frac{\hbar}{2\sqrt{2m^*\Phi_e}}, \tag{4}$$

where Φ_e is the electron tunneling barrier height at the SiO_2 interface. The distance z is estimated using following equations [3], [16]:

$$z = \lambda ln\left(\frac{-c_n(0)}{ln(0.5)2f}\right), \tag{5}$$

where

$$c_n(0) = v_{th}\sigma_{p/n}n_i. \tag{6}$$

The values used for material constants were as follows: $v_0 = 8\text{x}10^5$ m/s, taken from [9], [19], $n_i = \sim 10^{16}$ cm^{-3}, taken from [3], [20], $\sigma_{p/n} = 10^{-14}/10^{-16}$, $\Phi_e = 2.94$ eV, and $m_e^* = 0.41m_0$, taken from [16]. Values used in this study are the same as used in comparable studies on SWCNT transistors [3].

The general assumption behind charge pumping measurements is that the recombination current, I_{CP}, is dominated by the trapping at the SWCNT/SiO_2 interface, and that comparable numbers of electrons and holes are brought to the interface. However, this is not the case, since conduction in these devices is dominated by holes, and it is very difficult to bring a sufficiently large population of electrons to the surface in the bias ranges used. Additionally, since the SWCNTs in the transistors are unpassivated and the devices are measured in air, other trapping sites exist due to the adsorption of gas and water molecules on the SWCNTs and/or gate oxide surface, and these can contribute to the recombination current observed [3]. The non-uniformity of the SWCNT

distribution across the gate area, due to the fabrication method outlined previously, also adds to the potential error in estimating the trap density profile at the interface.

2.2 Carbon Nanotubes

A carbon nanotube (CNT) is described as an arrangement of carbon atoms in a tube structure, also described by rolling a planar sheet of carbon atoms all having their atomic bonds satisfied in a sp^2 planar configuration (graphene) [21]. Native defects exist in CNTs, though the defect density in most synthesized and purified CNTs is minimal.

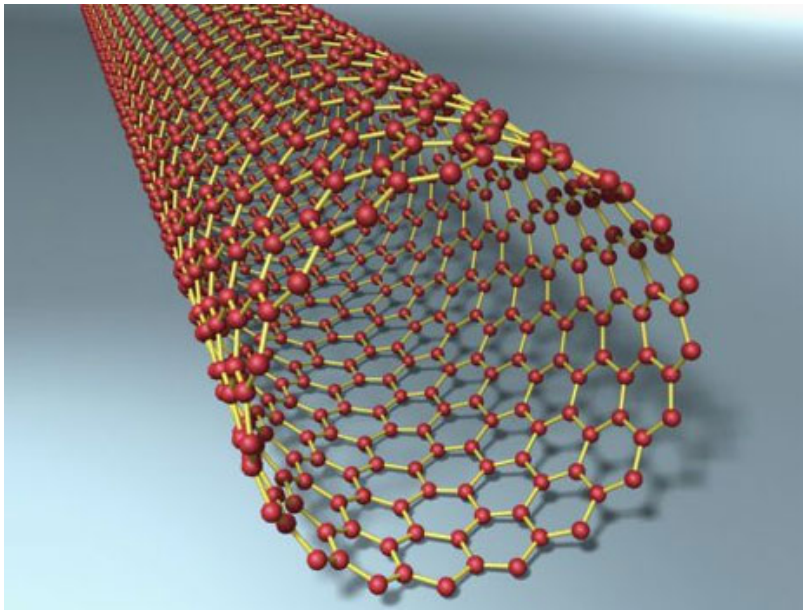

Figure 3: Wire diagram of carbon atoms depicting the rolled graphitic cylinder of sp^2-bonded carbon atoms. Reproduced with permission from Best [10].

Sumio Iijima is most commonly credited for the discovery of CNTs in 1991 while studying the material deposition on the cathode during the arc-discharge synthesis of fullerenes [1], [2]. The study was completed using transmission electron microscopy

(TEM), which showed a variety of closed graphitic structures [1], [21]. These structures had never been observed previously on this scale, opening the world to CNT research and sensationalizing the material that promised to revolutionize functional and non-functional materials alike with its unique properties [22]-[24]. A model of a basic SWCNT is shown in Figure 3.

2.2.1 Synthesis

Arc-discharge, laser ablation, and chemical vapor deposition (CVD) have been the three main processes for CNT growth. Both arc-discharge and laser ablation tend to produce large amounts of CNTs along with byproducts that require purification prior to device fabrication. CVD synthesizes the CNTs directly on a substrate [25].

Arc-discharge was the method used by Iijima in the synthesis and discovery of the first CNTs [1]. The main product of this process is a mixture of multi-walled carbon nanotubes (MWCNT) along with non-nanotube carbon and metal catalyst material. The removal of byproducts and purification is considered to be more expensive than synthesis itself [2]. This process uses two graphite rods separated by 1 mm that are enclosed in inert gas, such as helium or argon at low pressure. A dc arc voltage is applied under these conditions to generate fullerenes. However, when the anode graphite rod contains a metal catalyst MWCNT, SWCNT and pure graphite can be synthesized. Synthesis of MWCNTs has been further improved through the use of methane as a filler gas [2], [26].

Laser ablation is known for the synthesis of high quality SWCNTs, in terms of the diameter and growth control, with the ability to control SWCNT diameters by changing the furnace temperature, metal catalyst and flow rate of the gas. SWCNTs are synthesized by introducing a laser of carbon dioxide into a carbon composite doped with a metal

catalyst target enclosed in a tube furnace filled with argon gas. The target is vaporized during the synthesis process, resulting in the formation of SWCNTs that are carried into a collector due to the flow of inert gas [2], [25], [26].

CVD allows for the location and alignment of the synthesized CNTs to be controlled through the use of a metal catalyst to “seed” the CNT growth. A hydrocarbon gas is thermally decomposed in the presence of the metal catalyst in a furnace to grow the CNTs [2], [25], [26].

As synthesized, CNTs vary in their diameter and chiral angle and are produced along with impurities due to the synthesis of other carbon byproducts during each process. This leads to the necessity of a purification process to ensure the intended product is isolated. One process intended for the high purity separation of CNTs is a solution-based method using a surfactant. Separation is achieved using a bile salt such as sodium cholate, as a surfactant. This surfactant encapsulates every CNT with and the number of individual surfactant molecules required to surround the circumference the major determining factor in the buoyant density this density difference is based on the diameter of the CNTs. Ultra centrifugation of the solution is then applied to the solution resulting in a layer separation of CNTs by diameter as illustrated in Figure 4.

2.2.2 Semiconducting vs. Metallic Nanotubes

SWCNTs are distinguished based on three different physical properties of the individual nanotube: diameter, chirality and length. The chirality distinguishes between the two different transport mechanisms observed, resulting in semiconducting or metallic behavior. Metallic SWCNTs are observed to follow quantum transport as a conduction

mechanism, while semiconducting SWCNTs show Coulomb gap type conduction due to the Coulomb interactions between localized electrons [28].

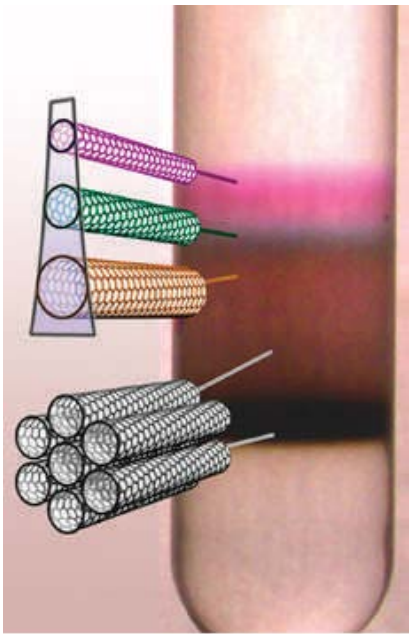

Figure 4: Illustration depicting the separation of CNTs by ultra-centrifugation. The optical contrast between layers observed is due to the correlation between the diameter of the CNTs and the magnitude of their band gap. Reproduced with permission from Arnold *et al.* [27].

The different chiralities of SWCNTs can be observed in Figure 5, which shows the three major chiral vectors resulting in armchair, chiral or zig-zag formations of the CNTs. The chiral vector is the axis about which the sheet of graphene would be rolled, defined by [29], [30]:

$$c_h = n_1 a_1 + n_2 a_2, \tag{7}$$

where a_1 and a_2 are the unit vectors between two crystallographically equivalent sites of the hexagonal graphene lattice, so a nanotube can be described by the pair of integers (n_1,n_2). When $2n_1 + n_2$ is observed as an integer multiple of three, the CNT exhibits

metallic conduction behavior, while for all other cases semiconducting behavior is observed. The zig-zag formation of SWCNTs or the (n_1,0) chiral vector results in metallic or semiconducting SWCNTs based on the relation previously outlined. Arm-chair (n_1,n_1) SWCNTs are always metallic. Other chiral vectors not described are chiral formations that result in semiconducting SWCNTs. A diameter-dependent relationship of the bad gap for semiconducting SWCNTs is [29], [30]:

$$E_{gap} = \frac{4\hbar v_F}{3d_{CNT}}, \tag{8}$$

where v_F is the Fermi velocity at $\approx 8\times10^5$ m/s [10], and d_{CNT} is the diameter of the CNT.

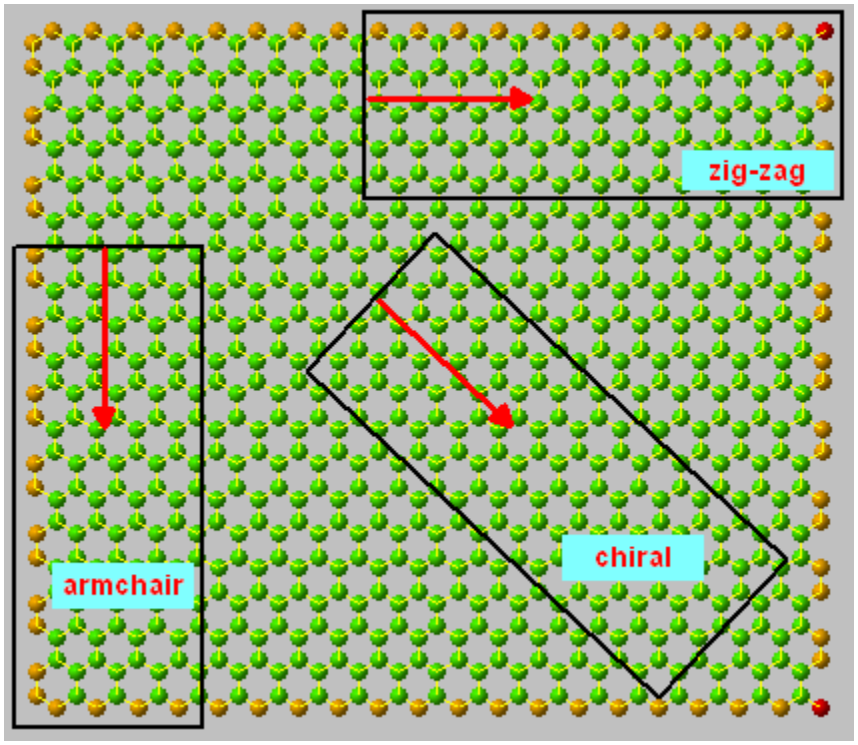

Figure 5: Planar wire diagram of sp^2-oriented carbon atoms or a sheet of graphene depicting the three major chiral vectors that separate the electronic properties observed in SWCNTs. The chiral vectors depicted are the vectors a sheet of graphene sheet would be rolled about to form a SWCNT. Reproduced with permission from Best [10].

2.2.3 Raman Spectroscopy

The Raman Effect occurs due to the inelastic scattering of monochromatic light incident upon a molecule, usually a laser. Only Raman active modes are observed. A Raman active mode is the resultant of the polarizability of a bond in a molecule where the polarizability must not be constant at the equilibrium position. Raman active modes can be both stretching and bending modes based on the molecular vibrations observed. The inelastic scattering of light is the cause of the vibration when light is absorbed by the molecule. When energy is absorbed, a difference in energy exists between the initial state and this new vibration state, which leads to a shift in the emitted photon's frequency relative to the initial monochromatic laser wavelength [31], [32].

If the final vibration state is more energetic than initial state, conservation of energy dictates that the photon emitted due to the molecular vibration be shifted to a lower frequency based on the Planck relation:

$$E = hcv, \tag{9}$$

where E is the energy in eV, h is Planck's constant, c is the speed of light, and v is the wavenumber of the Raman shift. This shift to a lower frequency is referred to as a Stokes shift, the commonly published and analyzed numbers. An Anti-Stokes shift is the result of the final vibrational state being of lower energy relative to the initial state, which results in a photon emitted at a higher frequency [31], [32].

In CNTs, the most notable vibrational modes observed are the radial breathing mode (RBM), *D*, *G*, and *G'* modes. Figure 6 depicts an example Raman spectra for metallic and semiconducting SWCNTs along with illustrations of the RBM and *G*

vibrational modes. The RBM is the vibration mode of the expansion and contraction of the cylindrical tubes and is particularly clear in high purity SWCNTs, while the *G* peak is attributed to the vibration modes observed in graphene or sp^2 carbon. The *D* peak is related to the chirality of the SWCNT and is the result of defects and asymmetry observed in a graphene sheet with an overtone of *G'*. These defects can come in the form of dislocations, Frenkel pairs, or non-ideal bonding structures in the CNT. The *G* peak is observable at 1582 cm^{-1}, which indicates interactions and vibrations down the long axis of the SWCNTs. The *D* peak is observable at 1350 cm^{-1}, with its *G'* overtone at 2700 cm^{-1} [31], [32], [33].

The location of the radial breathing mode is dependent on the diameter of the SWCNT (d_{CNT}) by [31]:

$$RBM_{peak} = \frac{248}{d_{CNT}}. \tag{10}$$

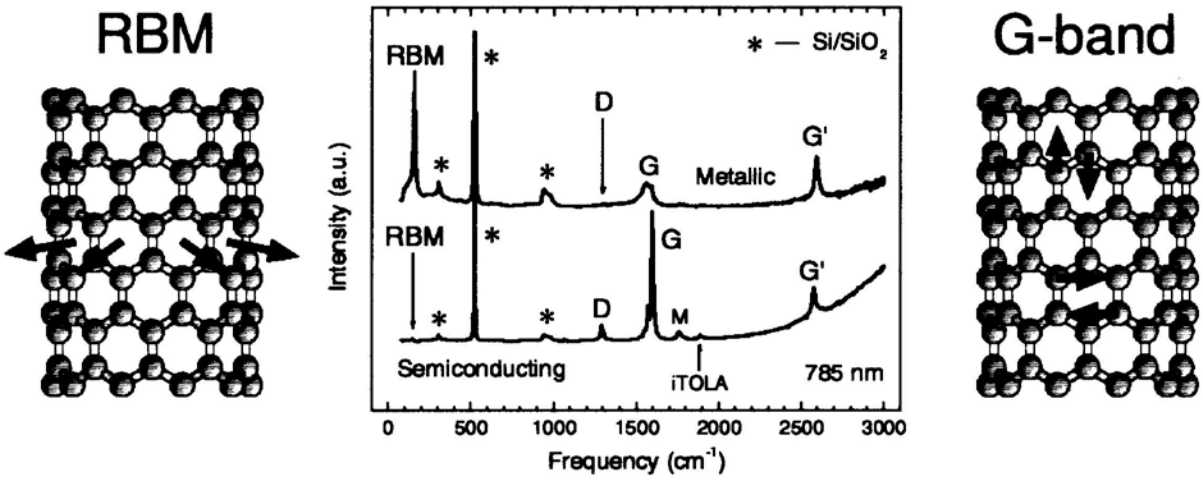

Figure 6: Raman spectra from metallic and semiconducting SWCNTs using a 785 nm laser, showing the key vibrational modes observable for SWCNTs. Illustrations depict the RBM and *G*-band, with arrows showing the directions of atom movement in each mode. '*' denote vibrational modes of silicon, the substrate used. Reproduced with permission from Dresselhaus *et al.* [31].

2.2.4 Annealing

Defects can occur in CNTs from several potential sources. Defects such as localized lattice defects (vacancies, substitutions, pentagon-heptagon defects and heterojunctions) are typically formed during synthesis or by intentional damage. Short- and long-range disorder can be induced due to electrostatic potential fluctuations created by charges in the substrate or adsorbates on the CNTs. Mechanical deformations, such as strains and twists both affect the local band gap and act as conductance barriers [34].

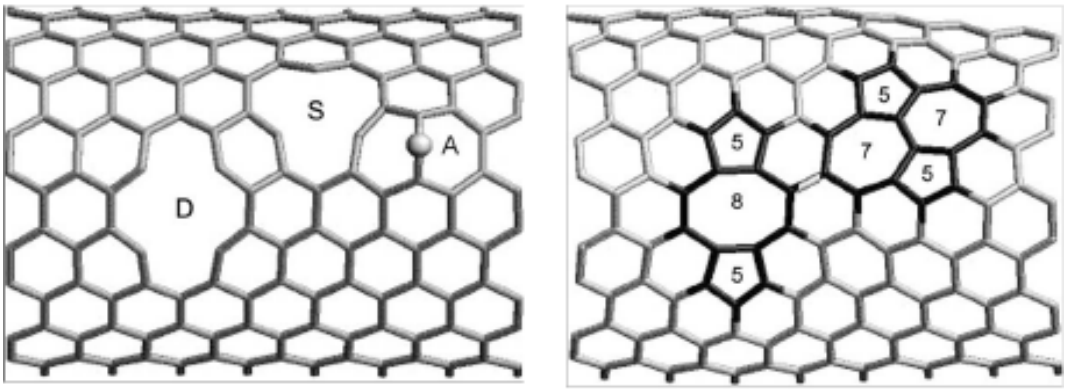

Figure 7: Illustration depicting defects (right) and defect annealing (left) in SWCNTs. During annealing the double vacancy (D), single vacancy (S) and the interstitial carbon atom (A) rearrange due to thermal excitation to reach a more stable bonding state with the reformation of the carbon network. Reproduced with permission from Krasheninnikov *et al.* [36].

Thermal-induced annealing in the SWCNTs has been observed at temperatures exceeding 300°C [35], [36]. This defect annealing is governed by two mechanisms. The first mechanism is the healing of vacancies present, introduced either during synthesis or through radiation damage in this case, through the saturation of dangling bonds by forming non-hexagonal rings. The second annealing mechanism is the migration of carbon interstitials. Interstitials are atoms not in normal bonding positions that are capable of migrating or diffusing due to thermal energy in the system until reattaching at

a vacancy. Figure 7 illustrates single, double and interstitial defects and their possible recombination paths [36].

2.3 Carbon Nanotube Transistors

2.3.1 Theory

The dominant factor in the switching mechanism for SWCNT field-effect transistors is the Schottky barriers that forms at the SWCNT-metal contacts, while ballistic transport is assumed along the SWCNT conduction path. The Schottky barrier in this sense accounts for the band bending in a semiconductor at the semiconductor/metal interfaces [30], [37]. This barrier is formed based on the difference between the Fermi level of the metal contact and valence/conduction band in the SWCNT semiconductor. This barrier becomes variable due to the variability in the band gap of a SWCNT based on the nanotube diameter, so different nanotube diameters will result in different SWCNT band gaps and different barrier heights at the metal-SWCNT interface [37]. Figure 8 illustrates the presence of the Schottky barrier for different gate contacts.

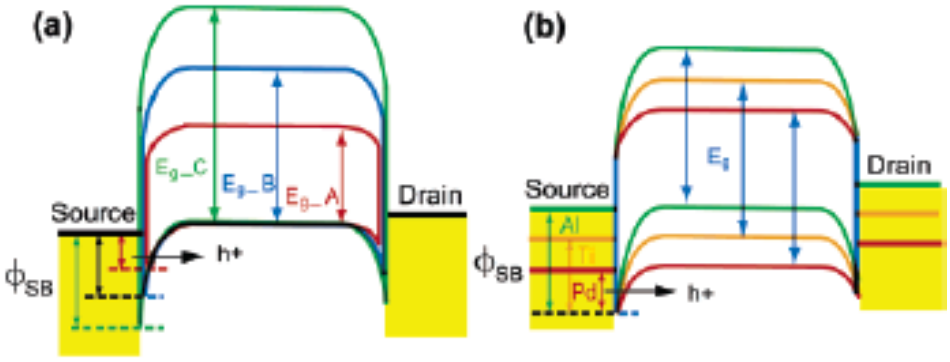

Figure 8: (a) Illustration of the band diagram with the Schottky barrier difference for different nanotube diameters, using the same metal at both contacts. (b) Illustration the Schottky barrier difference using different metals at each contact with a uniform carbon nanotube diameter. Reproduced with permission from Chen *et al.* [37].

The nanotube diameter variation results in a large current variation in device-to-device performance, while the Schottky barrier at the metal contacts forms a constant depending on the metal contact used and asymmetry of the saturation currents can be induced by the use of different metals at each contact.

Undoped SWCNT transistors are observed to be ambipolar devices. However oxygen is readily adsorbed to the SWCNT surface when exposed to air, which results in a p-type doped transistor [30], [38], [39]. The oxygen adsorbed to the SWCNT surface acts as charge trapping centers, while it is also assumed that oxygen is a hole donor. Charge trapping centers could result in the suppression of the electron channel formation [39]. N-type transistors can also be fabricated through exposure to potassium [38] or hydrogen [40] gas. The fabrication of both p- and n-type transistors is important to the use of SWCNT transistors in complementary logic devices and circuits.

2.3.2 Design/Structure

SWCNT field-effect transistors have been fabricated in several different designs similar to that of silicon-based transistors, such as a back- or top-gated transistor, and in more unique designs, such as wrap-around gated and suspended transistors [38].

Back-gated SWCNT transistors are the most simplistic transistor design where the SWCNTs are deposited onto a prefabricated series of source and drain contacts over a gate oxide, while the substrate acts as a common gate for all transistors on the substrate. The most common substrates are silicon with a silicon dioxide gate oxide. This does not allow for the individual switching of transistors in current designs, and with lay-down methods for depositing the SWCNT across the source and drain contacts, a significant contact resistance between the SWCNT and metal exists [38]. Fabrication changes have

been made to reduce the contact resistance by depositing the source and drain contacts onto a patterned SWCNT film [4], or by growing the SWCNT across the source and drain to form aligned networks of SWCNT transistors [40], [41], [42]. Back-gated designs expose the SWCNT to atmospheric conditions, allowing for water and oxygen to adsorb to the SWCNT, thereby changing electrical properties.

Top-gated transistors are fabricated utilizing similar methods to back-gated transistors, where transistors are commonly fabricated on top of a silicon substrate with the source and drain contacts. A gate dielectric is deposited over the SWCNT gate area prior to the deposition of the top gate contact [41], [42]. Individual isolated gates for each individual transistor allows for the switching of each transistor independently, which is not available to a device with a common gate. Due to the ability to control the thickness of the deposited gate dielectric, a larger electric field can be generated using a lower voltage with thinner gate dielectrics. With a top gate dielectric, this allows for both p- and n-type transistors. N-type transistors require a passivation layer to prevent oxygen from adsorbing to the SWCNT surfaces that can also function as a barrier by fixing phosphorous or hydrogen adsorbed to the SWCNT surfaces.

Wrap-around gated SWCNT transistors were developed to improve the electrical performance of SWCNT transistors by depositing the gate dielectric and contact around the SWCNT. The gate dielectric and contact are etched off at the ends to provide a source and drain contact. This design was developed to reduce leakage currents and improve device on/off ratio. Suspended SWCNT transistors involve suspending a SWCNT over trenches so the SWCNT only comes into contact with the gate to reduce scattering at the interface [38].

As devices scale down, the use of silicon dioxide as a gate dielectric limits the size of a transistor due to its relatively low dielectric constant (κ). In order to continue scaling down, high-κ materials such as zirconium oxide and hafnium oxide are required to provide high capacitance without relying on small film thickness [41].

2.3.3 Hysteresis

Issues exist with SWCNT field-effect transistors that use a back gate design for the ease of fabrication. Exposure to gases and water allows for the adsorption of molecules onto both the exposed SWCNT and gate oxide surfaces. The adsorption of these molecules has been shown to affect the current-voltage characteristics of SWCNT field-effect transistors by creating a significant gate hysteresis [43]-[47].

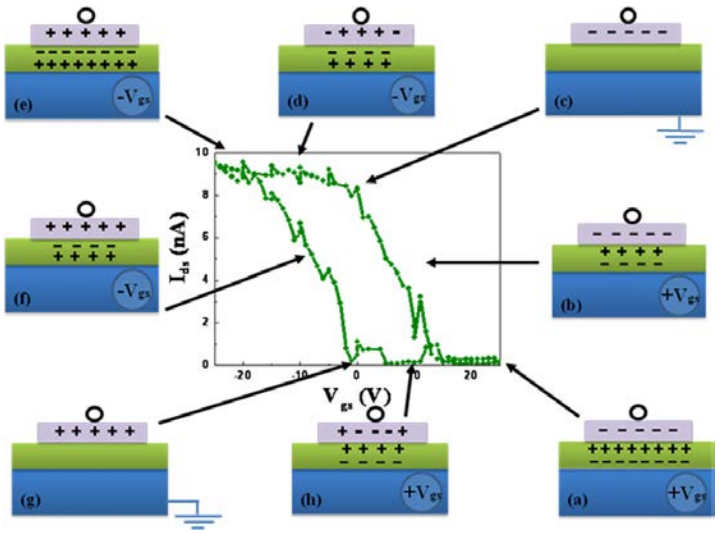

Figure 9: Illustration depicting the dynamic screening effect of injected charges. Holes or electrons are injected into traps based on the gate bias applied. Reproduced with permission from Ong *et al.* [43].

Water molecules are known to function as trapping centers that readily adsorb to SWCNT and SiO_2 surfaces [44], [45]. Defect locations in the gate oxide, such as in the

bulk or at the surface, also play a role in the hysteresis observed [43], [46]. Bulk defects cannot be mitigated using surface passivation, which is the most common technique used to reduce transistor hysteresis and increase the device-to-device consistency [46], [47]. Figure 9 illustrates a model describing the process of charge injection from the SWCNT into the surrounding materials (adsorbate and gate oxide traps) based on the gate bias.

The sole source of hysteresis has been isolated to the carbon nanotubes alone and surface passivation has been employed to remove the hysteresis observed through several methods. Hysteresis reduction has been achieved through by using a bottom dielectric with a molecular monolayer and by deposition of an oxide on top of the SWCNT. Hydrophobic self-assembling monolayers applied in a vacuum environment have been used to greatly improve transistor hysteresis and consistency [47].

2.4 Radiation Effects

2.4.1 Proton Damage Effects

When a target is struck by a highly energetic charged particle, such as a proton, electron, or heavy ion, varying mechanisms for the energy and momentum transfer exist. These mechanisms are broken into both primary and secondary effects, the primary effects are:

- Electron excitation or ionization of individual atoms,
- Collective electronic excitation, *e.g.*, plasmons,
- Breakage of bonds or cross-linking,
- Generation of phonons, leading to heating of the target,
- Displacement of atoms in the bulk of the target

- Sputtering of atoms from the surface.

And secondary effects such as:

- Emission of photons,
- Emission of secondary or Auger electrons, leading to a charging of the target.

The relative importance of each of the possible primary and secondary effects are highly dependent on the cross section of interaction for each respective interaction based on the material or atoms themselves [48]. When considering radiation damage to carbon and SiO_2-based devices, it is useful to differentiate between radiation damage effects that lead to a displacement of atoms or knock on damage, and excitation or ionization reactions.

The primary defects generated in a crystalline solid or an ordered molecular solid are a combination of vacancies and interstitials in the lattice. Vacancies are the absence of an atom from its expected lattice position, while an interstitial is the displacement of an atom into a non-lattice position. A Frenkel pair is the combination of a vacancy and its adjacent interstitial [49].

2.4.2 Silicon Damage

Displacement damage in solids, such as silicon-based materials, is determined analytically through the non-ionizing energy loss (NIEL) rate. Frenkel pairs and phonons are generated as a part of the energy introduced via elastic and nuclear inelastic interactions. *NIEL* can be calculated as follows:

$$NIEL = \left(\frac{N}{A}\right)[\sigma_e T_e + \sigma_i T_i], \tag{11}$$

where N is Avogadro's number, A is the atomic weight of the target material, σ_e is the total elastic cross section, σ_i is the total inelastic cross section, and T_e and T_i are the elastic and inelastic effective average recoil energies corrected for ionization loss, respectively [49].

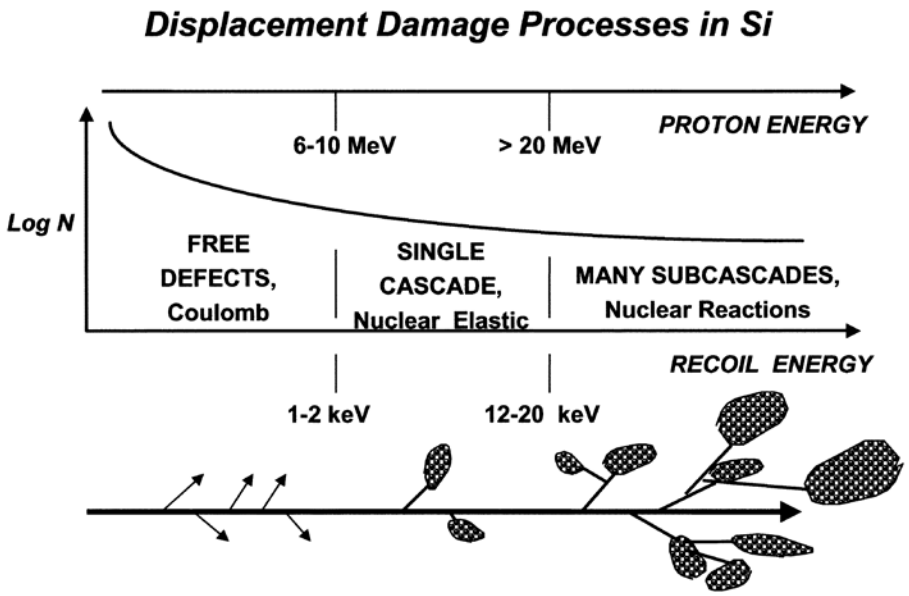

Figure 10: Illustration relating the energy of incident protons into a silicon-based material to the frequency and extent of the knock on effects categorized as free defects, single cascades and many cascades. Reproduced with permission from Srour *et al.* [49].

Figure 10 illustrates the initial defects generated following a knock on effect using protons of varying energies. Based on the incident proton energy in the silicon material, a variety of initial damage effects are possible: free defects, single cascades, and multiple cascades. A free defect refers to the generation of a Frenkel pair. With increasing proton energy, the potential amount of energy imparted upon an individual silicon atom is increased, allowing for cascade effects where the displaced silicon atom displaces other

atoms due to the momentum it gains. This ignores annealing or defect reordering of the generated Frenkel pair and its location. [49].

Ionizing radiation creates electron-hole (e-h) pairs in the SiO_2 gate oxide for MOS capacitors and transistors. Relative to the holes generated in the valence band, electrons in the conduction band are found to be extremely mobile in SiO_2. Initial recombination refers to the process of the electrons and holes immediately recombining following ionizing radiation exposure. However, a highly electric field-dependent process exists where a fraction of the holes remain unrecombined. This process can be expressed given the following equation [50]:

$$N_h = f(E_{ox}) g_0 D t_{ox}, \tag{12}$$

where N_h is the total number of holes generated that escape initial recombination, $f(E_{ox})$ is the hole yield expressed as a function of the electric field, g_0 is the material dependent charge pair density given per rad for SiO_2, D is the total dose, and t_{ox} is the thickness of the oxide. The fraction of uncombined holes generated for varying ionizing radiations is shown in Figure 11 [50].

Holes generated can be trapped in both the SiO_2 bulk and at the interface region of the MOS device, forming a positively charged oxide trap. Another explanation for the positive charge build up in the oxide is that hydrogen ions are likely released by holes that then “hop” through the oxide or remain trapped in the bulk or near the interface. Near the interface, oxygen diffusion generates oxygen vacancies that form as trapping centers for holes and hydrogen alike [50].

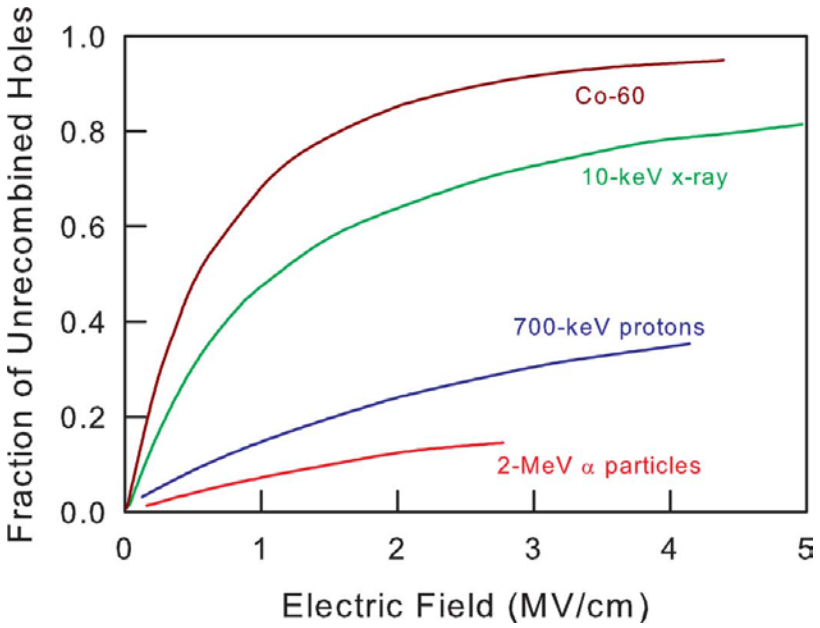

Figure 11: Fraction of uncombined holes as a function of the applied electric field for gamma rays, x-rays, low-energy protons and alpha particles. Reproduced with permission from Schwank *et al*. [50].

The trapping probabilities of both electrons and holes in silicon materials have been studied as a function of the proton fluence. Effective trapping probabilities are a linear function of the proton fluence, and the trapping probabilities are independent of oxygen exposure and the silicon resistivity [51].

2.4.3 SWCNT Damage

A wide variety of proton energies and fluences, along with electrons and other ions, have been explored in studies to determine the overall level of damage to SWCNTs and their physical and electrical properties through a variety of testing methods [7], [52]-[57]. Curving of the SWCNTs, formation of short pieces, and an eventual complete amorphization of the SWCNTs have been observed after 2 MeV and 3 MeV proton irradiation, confirmed through both TEM and resistivity measurements [52]. A linear

increase in the resistivity was observed, up to the onset of SWCNT degradation, for 2 MeV proton irradiations.

Beginning with low energy proton irradiations, 100 keV protons induced no observable damage to SWCNT networks with fluences up to 1×10^{14} protons/cm^2, confirmed through both Raman spectroscopic measurements comparing the *D/G* peak ratios, and Hall Effect measurements of the sheet resistivity [53]. The optical properties of SWCNTs matrixed in poly(3-octylthiophene) were investigated following proton irradiations with 2 MeV protons in a fluence range of 5×10^{10} to 5.6×10^{15} protons/cm^2. Optical absorption results indicated that there was little effect on the intraband transitions in the SWCNTs. However, a broadening of the spectra and decrease in the SWCNT radial breathing mode could be attributed to radiation-related degradation of the SWCNTs [54]. High energy proton irradiations, 10 and 20 MeV, at fluences up to 4×10^{12} protons/cm^2, revealed no significant change in the SWCNTs, verified through a comparison of the *D/G* peak ratio [55].

Irradiations involving alpha particles, ions and gamma rays have shown more significant radiation-induced damage to SWCNTs and graphene [7], [56], [57]. Alpha irradiations up to a fluence of 3×10^{12} particles/cm^2 resulted in a significant decrease in the SWCNT conductivities, as shown in Figure 12.

Similar results were observed for gamma irradiations up to 505 kGy, 1×10^{15} boron ions/cm^2, and 5×10^{14} phosphorous ions/cm^2; both with energies of 150 keV, and 35 keV carbon ions. Significant increases in the *D/G* peak ratios were observed using Raman spectroscopic measurements [56], [57]. This increase in SWCNT damage as a function of the increasing ion fluence is shown in Figure 13.

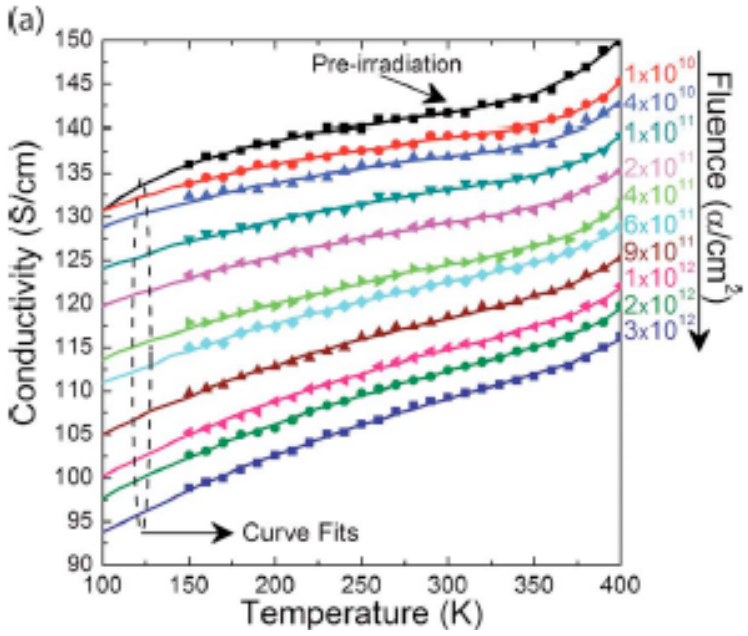

Figure 12: Temperature-dependent conductivity measurements as a function of alpha fluence on SWCNT film samples showing a decrease in the conductivity with increasing radiation fluences. Reproduced with permission from Cress *et al.* [8].

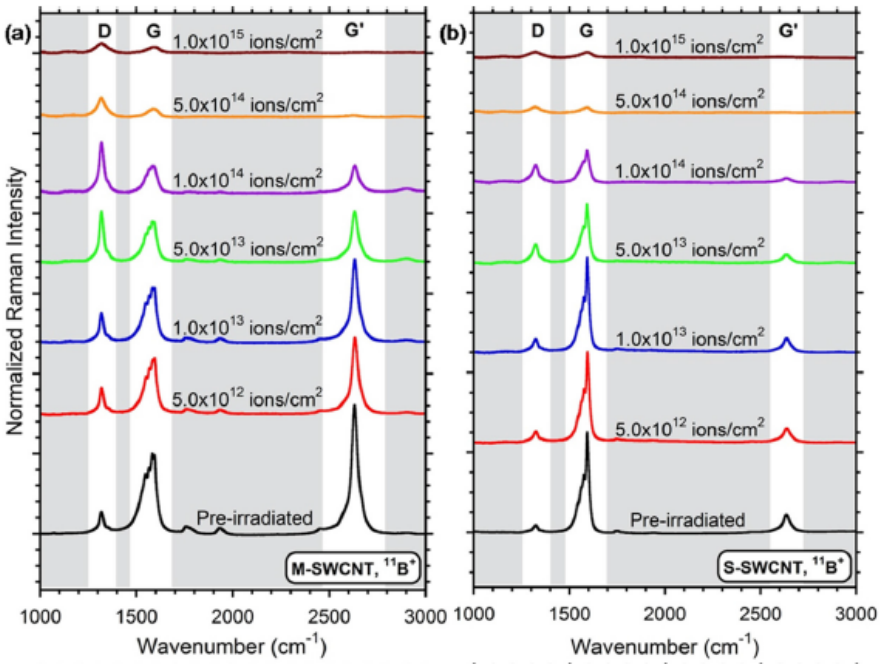

Figure 13: Raman spectra for both SWCNT and MWCNT thin films as a function of the increasing ion fluences for 150 keV boron ions. Reproduced with permission from Rossi *et al.* [6].

2.4.4 Previous Research – SWCNT FET

A significant amount of research exists on SWCNT physics, devices and radiation effects. This thesis follows the research of Francis [3], Cress [5], [8] and Best [10]. These papers use the same SWCNT material produced by NanoIntegris as in this research, along with similar SWCNT device designs and characterization techniques. Interest in Raman spectroscopy stemmed from research by Best [10], which is based on the correlation between significant radiation damage due to increasing ion fluence on SWCNT thin films by Rossi *et al.* [6].

Similar to this research on proton irradiation of SWCNT transistors, Francis *et al.* irradiated samples using 1 MeV electrons to fluences of 1×10^{16} to 1×10^{17} electrons/cm^2 producing Raman spectra as shown in Figure 14. This figure demonstrates the expected results for this research in agreement with results by Rossi *et al.* and Best. Charge pumping measurements were also carried out by Francis *et al.* on transistors of a similar design. Charge pumping is a standard method used to determine the interface trap density as a function of the distance from the interface for MOS devices. Results of this study are shown in Figure 15.

Current-voltage characterization is a standard measurement used to determine the device performance of silicon-based MOS transistors and SWCNT transistors alike [50], [3], [5]. Figure 16 illustrates results of current-voltage measurements by Francis *et al.* on SWCNT transistors with an Al_2O_3 gate oxide [3]. Similar results are expected for the devices used in this study, given the hole trapping generally observed in irradiated SiO_2 gate oxides. This agrees well with studies using high energy protons [4] and low energy electrons [9], where decreases in the drain current were observed. A significant goal of

this research is to correlate the amount of proton radiation damage to the changes in the Raman spectra, interface trap density, current-voltage characteristics, and the device performance.

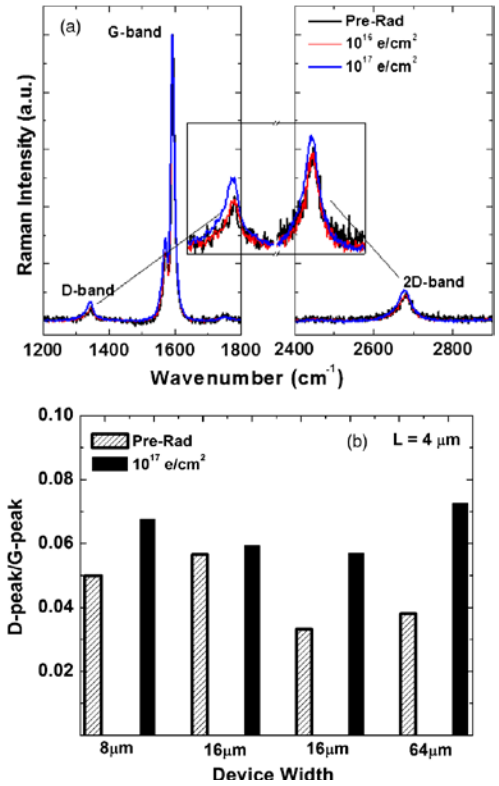

Figure 14: Raman spectra presented before and after irradiation (top), along with the *D/G* ratio as a function of channel width (bottom). Reproduced with permission from Francis *et al.* [3].

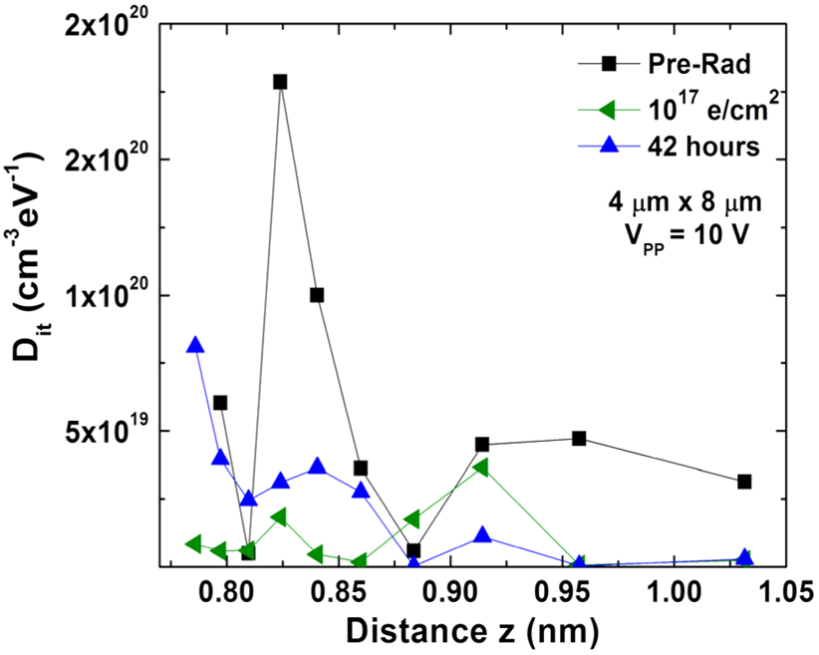

Figure 15: Interface trap density as a function of distance from the SWCNT/gate oxide interface before and after irradiation and annealing. Reproduced with permission from Francis *et al.* [3].

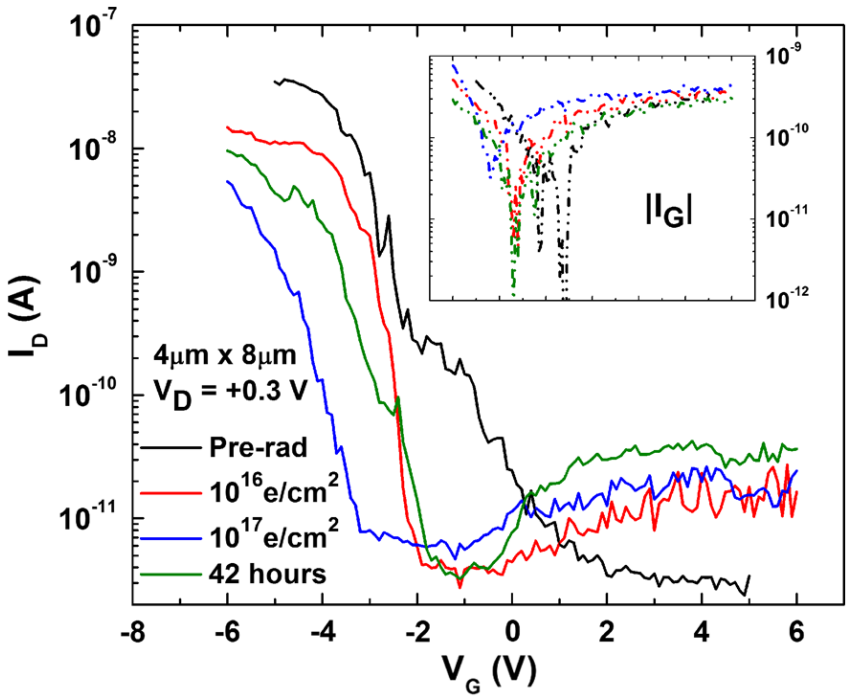

Figure 16: Drain current and gate current magnitude as a function of the applied gate voltage before and after electron irradiation. Reproduced with permission from Francis *et al.* [3].

III. Experiment

3.1 Purpose

The objective of this research was to investigate the effects of proton irradiation on the overall performance of SWCNT transistors using Raman spectroscopy, charge pumping and current-voltage characterization measurements. Of particular concern was understanding how the protons affected the properties of the SWCNTs, the electrical characteristics of the substrate, and the overall device performance. The transistor fabrication and design is described first, followed by the experimental equipment descriptions. The experimental procedures and methods of data acquisition and analysis that were used in this research concludes this chapter.

3.2 Experiment Setup and Design

3.2.1 Transistors

The carbon nanotube transistors used throughout this study were fabricated by the Naval Research Laboratory. SWCNTs used as the semiconducting material to fabricate the transistors were obtained as a powder from NanoIntegris, Inc. Both 98% IsoNanotube-S (semiconducting SWCNTs) and 98% IsoNanotube-M (metallic SWCNTs) were used for the two different device types. All SWCNTs produced by NanoIntegris, Inc. are grown using the arc discharge method outlined in the previous chapter. The nanotube diameters range from 1.2 to 1.7 nm and their lengths range from 100 nm to 1000 nm. Two chips, each containing hundreds of transistors, were fabricated

using different SWCNT mixtures: 100% semiconducting SWCNTs and a 50/50 mixture of semiconducting and metallic SWCNTs. Figure 17 shows the general design for the SWCNT transistors.

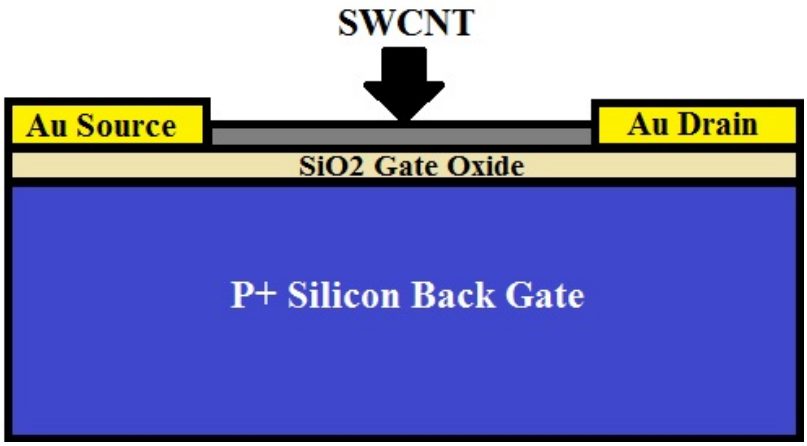

Figure 17: Diagram representing a cross section of the back-gated CNTFET design.

SWCNTs were suspended in an aqueous solution of 1% w/v sodium dodecyl by horn sonication for 20 minutes. Following sonication, the SWCNTs were vacuum filtrated through a 0.2 micron mixed cellulose ester (MCE) membrane until almost dry. Residual surfactant is washed away with purified water until a clear stream of water is passing through the vacuum filter. The film and MCE membrane were washed though several acetone baths for a duration of 20-30 minutes to ensure that the MCE membrane was completely dissolved before a final wash in a cleaner solvent such as methanol [58]. The resulting thin film is transferred to the substrate by lifting out the film using the substrate as a base. The substrate consisted of a p-type silicon substrate with a resistivity of 1-10 ohm-cm and a 14-20 nm layer of SiO_2 on the silicon for the gate oxide.

SWCNT network channel regions were formed using photolithographic patterning using a Shipley S1811, and were isolated using a 10 second O_2 plasma etch. The photoresist was stripped using an acetone wash followed by a 2 hour heat treatment at 300°C in air. Source and drain contacts were deposited via electron beam evaporation beginning with a 20 Å layer of titanium, followed with 380 Å of gold. Each reticle consists of transistors of different channel width and length, varying from 2 to 64 µm and 4 to 128 µm, respectively, in steps of powers of 2 µm, resulting in 36 devices per reticle [5]. Figures 18 and 19 depict the semiconducting transistor chip along with an example reticle.

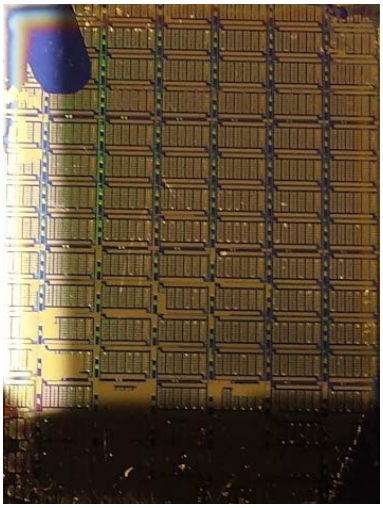

Figure 18: The semiconducting SWCNT chip depicting the total number of reticles fabricated on a single chip. Only the center reticles contained devices due to the SWCNT film size.

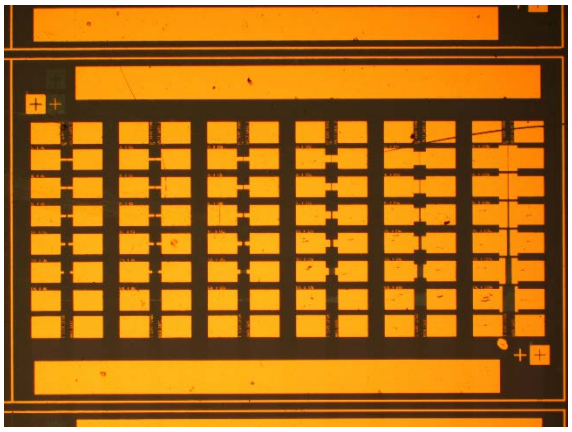

Figure 19: A single transistor reticle with the 10× objective of an optical microscope, depicting the 36 unique transistor devices present in each reticle. The channel length and width differences can be observed clearly.

Chips were taken to the Air Force Research Laboratory Sensors Directorate to dice each chip into individual reticles. Chips were adhered to a UV curable dicing tape to secure the chip to the base plate for dicing. Dicing was performed by Sensors Directorate staff using a diamond blade rotating at high speed. Samples were numbered based on the chip type (semiconductor or semiconductor/metallic), along with the column and row designation. Semiconducting SWCNT transistors were labeled as EKS01, while the semiconducting/metallic SWCNT transistors were labeled as EKSM01, followed by the row and column designation in the form of C3R5, for example.

3.2.2 Current-Voltage Characteristics

All *I-V* curves were measured before and after irradiation, and were collected using a Keithley 4200 Semiconductor Characterization System and Signatone probe station. Samples were mounted to the stainless steel back plate of the Signatone probe station, which acts as the common back gate for all transistors, as shown in Figure 20. Each transistor is tested individually using tungsten probes to make connection to the

source and drain. The probes are each connected to an individual source-measurement unit (SMU) in the Keithley 4200-SCS.

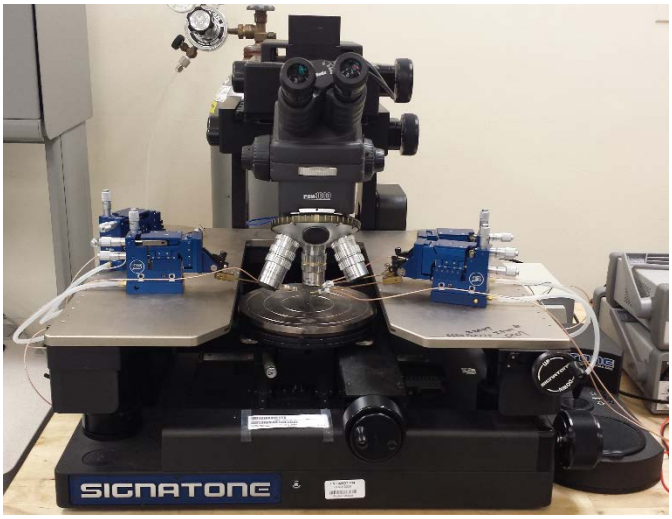

Figure 20: The Signatone probe station used to test individual transistors for both current-voltage characterization and charge pumping measurements. The Keithley 4200-SCS and Agilent 33220A connect directly to the probes via coaxial cables.

Current-voltage measurements were made by applying +0.3 V to the drain contact, 0 V to the source contact, and sweeping the gate voltage from -5 to +5 V in 0.1 V steps while measuring the drain current [3]. An example of a dual-sweep current-voltage (*I*-*V*) measurement is shown in Figure 21 for a semiconducting SWCNT transistor depicting the general on/off characteristics and significant hysteresis observed in all samples. The same settings and parameters were used for both EKS01 and EKSM01 samples. From these measurements, parameters such as device threshold voltage and hysteresis voltage are determined for each device, and are used to characterize device response as a function of radiation, as discussed below.

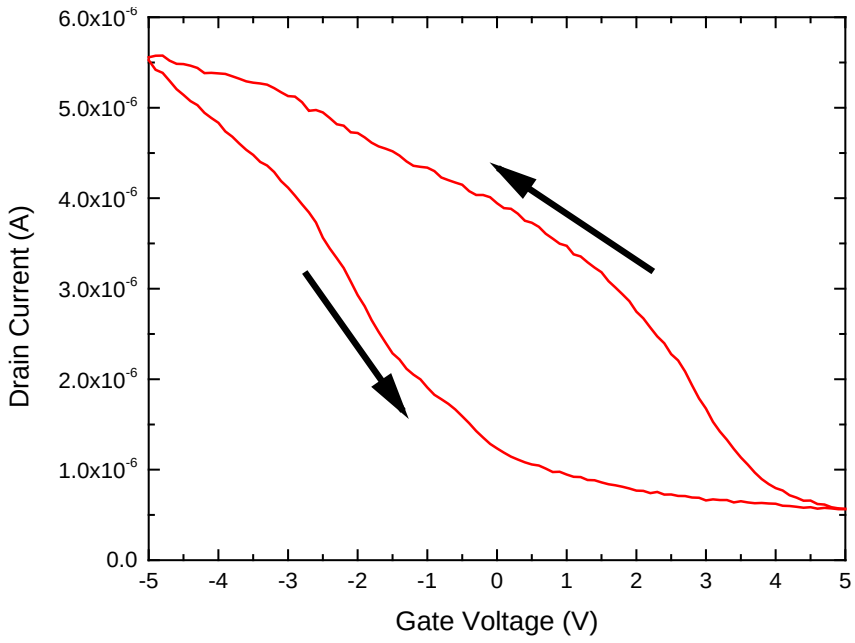

Figure 21: Representative *I-V* curve of a semiconducting SWCNT transistor on a linear plot.

Prior to and following irradiation, the threshold voltage was determined for each transistor by finding the intersection of a line fit to the linear region on the reverse sweep of the *I-V* curve, with the drain current measured at a -5 V gate bias, as illustrated in Figure 22 below. Subtracting the pre-irradiation threshold voltage from the post-irradiation threshold voltage yields the threshold voltage shift due to radiation damage.

The hysteresis voltage was determined by measuring the gate voltage difference between identical drain current values on the forward and reverse *I-V* sweep, as indicated in Figure 23. For each transistor, the relative change in hysteresis with irradiation was determined at a drain current level that was 5 % from the on-state, 5 % from the off-state, and 50 % from the off-state. A significant reduction in drain current was also observed after irradiation for these devices, as shown in Figure 23. This drain current reduction, or downshift of the *I-V* curve, due to radiation damage was determined for each transistor by

calculating the difference in drain current between pre- and post-irradiation values at drain current levels measured at 50% of the on-state level.

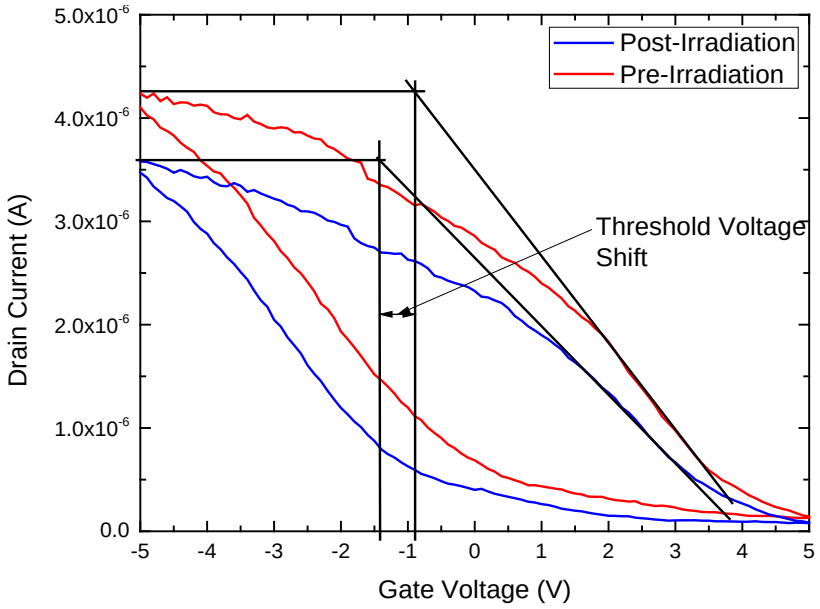

Figure 22: Drain current as a function of gate voltage for the semiconducting SWCNT transistor EKS01, before and after irradiation, illustrating the method used to determine the threshold voltage shift.

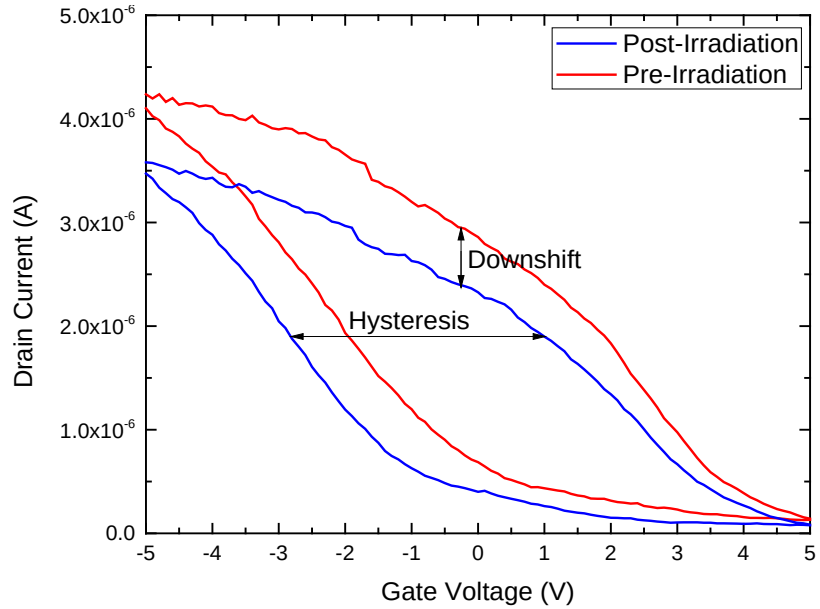

Figure 23: Drain current as a function of gate voltage for the semiconducting SWCNT transistor EKS01, before and after irradiation, illustrating the reduction in drain current and hysteresis.

The gate leakage current was also monitored before and after irradiation. In general, the measured gate current is due to carriers that tunnel through the oxide barrier and into the gate, and ideally, should be significantly lower than the measured source and drain currents. For these devices, the gate leakage current was compared before and after irradiation to determine if there was a significant increase in the leakage current due to radiation damage in the oxide. Additionally, these measurements were used to confirm that the gate leakage did not significantly affect the charge pumping current measured at the source and drain contacts, and that any decrease in either the charge pumping current or drain current was not being lost through the gate contact.

3.2.3 Charge Pumping

Charge pumping measurements are non-destructive measurements that aid in quantifying the charge trapping present in the gate oxide, and are used in this study to characterize the radiation-induced damage in these SWCNT transistors. Originally devised for use with MOS capacitors, the method was revised by Groeseneken *et al.* [15] in 1984 to apply to MOS transistors. Two of the charge pumping techniques that are used in this study are the variable amplitude technique and the variable frequency technique. Both techniques require the use of a function generator to generate a square pulse on the gate of the device while grounding the source and drain, and measuring the current generated at the drain.

Charge pumping measurements were carried out using a Keithley 4200-SCS as a data collection and measurement unit, while a voltage pulse was applied to the gate using an Agilent 33220A 20 MHz/Arbitrary Waveform Generator. This experimental setup is shown in Figure 24. For these measurements, a square-wave pulse was used, with a peak-

to-peak voltage, V_{PP}, of 2 V (±1 V). The frequency of the pulse was varied from 10 kHz to 1 MHz, and the recombination current at each frequency was measured at the source and drain contacts, which were biased at 0 V during the measurements. Originally, V_{PP} was set at 10 V, but was reduced to 2 V after all transistors tested at 10 V were destroyed.

Prior to irradiation, 3 reticles were measured to determine an average of the SWCNT/SiO_2 surface trap density profile in the oxide. Following irradiation, the same test set up was used. However, all irradiated reticles were measured to determine an average surface trap profile for each proton fluence, to compare to the pre-irradiation average. Figure 25 shows a plot of the charge recombined per cycle, Q_{CP}, as a function of frequency for an unirradiated semiconducting SWCNT transistor.

By taking the derivative of Q_{CP} as a function of the frequency, and using equation (1) given in Chapter 2, the interface trap density can be determined as a function of distance from the CNT/oxide interface.

Error bars are calculated using the standard deviation of the calculated interface trap densities across all transistors on a reticle. Standard deviation (s_N) is calculated using:

$$s_N = \sqrt{\frac{1}{N}\sum_{i=1}^{N}(x_i - \bar{x})^2}, \tag{13}$$

where N is the number of samples, x_i is the interface trap density of the current sample, and $\bar{x}$ is the average interface trap density across all samples.

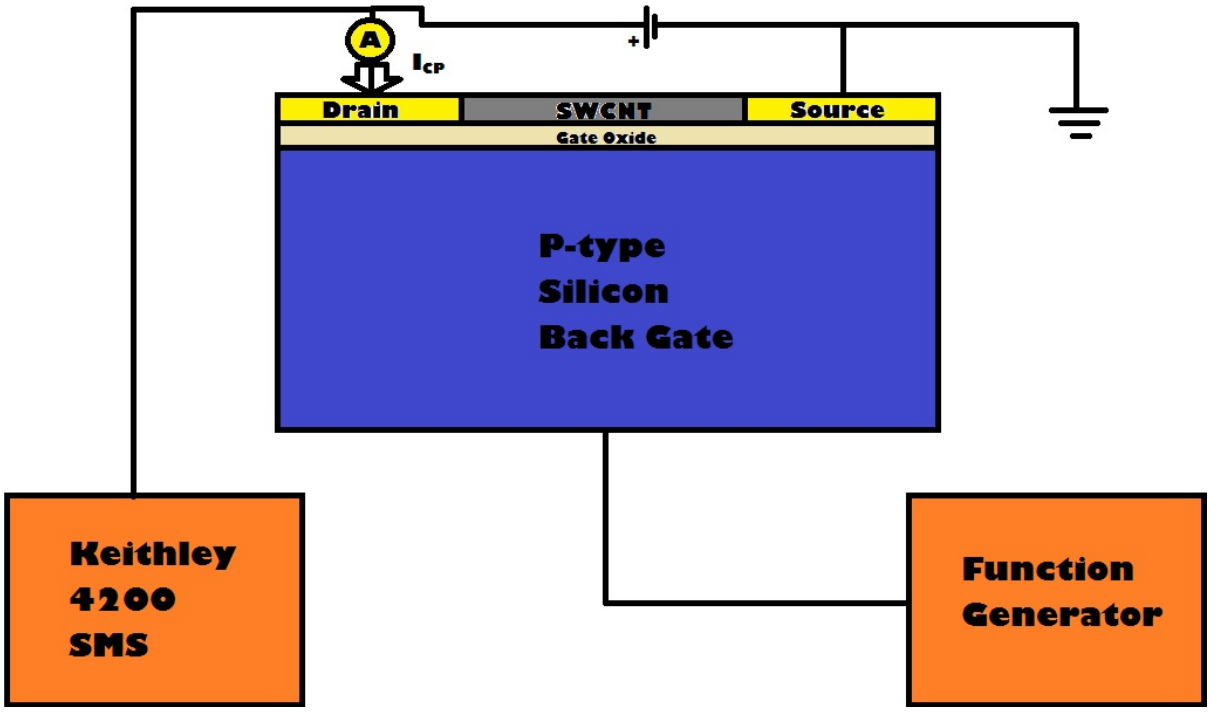

Figure 24: Experimental setup for charge pumping measurements. A positive bias is placed on the drain, where the current is measured as the charge pumping current I_{CP}. The gate is pulsed between inversion and accumulation using a function generator.

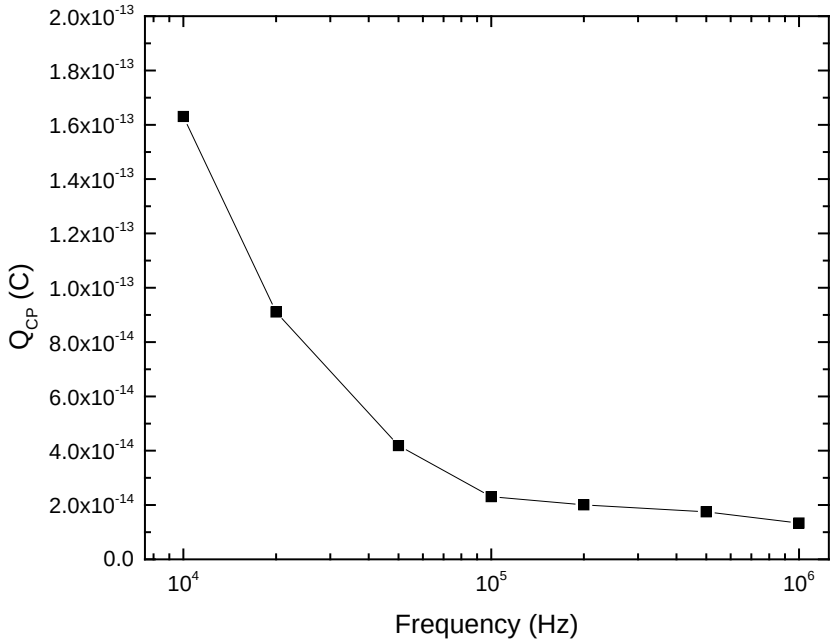

Figure 25: Charge pumped per cycle, Q_{CP}, as a function of frequency for a semiconducting CNT transistor using a peak-to-peak voltage, V_{PP}, of 2 V. Gate area dimensions are 2 µm long by 128 µm wide.

3.2.4 Raman Spectroscopy

The purpose of the Raman study was to quantify the radiation damage in the SWCNTs separately from the damage induced in the substrate, as a function of the proton fluence. All Raman spectroscopic measurements were collected before and after irradiation, using a Renishaw inVia Micro Raman system at the Air Force Research Laboratory Materials and Manufacturing Directorate. These measurements were made using a 514.5 nm laser, at either 10 or 100% of the full laser power (21 mW), depending on the intensity of the SWCNT *D* and *G* modes observed using the 50× microscope objective lens. The 514.5 nm laser was chosen based on previous studies on the electron damage to SWCNT devices [10]. The system was set using an extended grading scan type with the 1200 l/mm to provide the most extensive spectrum scan. The spectrum range scanned for all measurements was from 100 to 2000 cm^{-1} to include the characteristic peak for silicon, along with the *D* and *G* peaks for the SWCNTs. A representative spectrum of the semiconducting and semiconducting/metallic SWCNT transistors are shown in Figures 26 and 27, respectively. Apparent differences observable between Figures 26 and 27 are due to the difference of SWCNT density between the two mixtures. A higher intensity *G* band relative to the characteristic silicon peak can be attributed to a higher density of SWCNT present in the thin film spanning the gate area.

For the purpose of comparing different Raman spectra, the background spectrum was subtracted using a linear fit before normalizing the intensity to the *G* peak for each spectrum. This data manipulation is required since the background due to the reflected laser into the detector, the laser power settings, laser focus, and accumulation time is not identical in every single measurement.

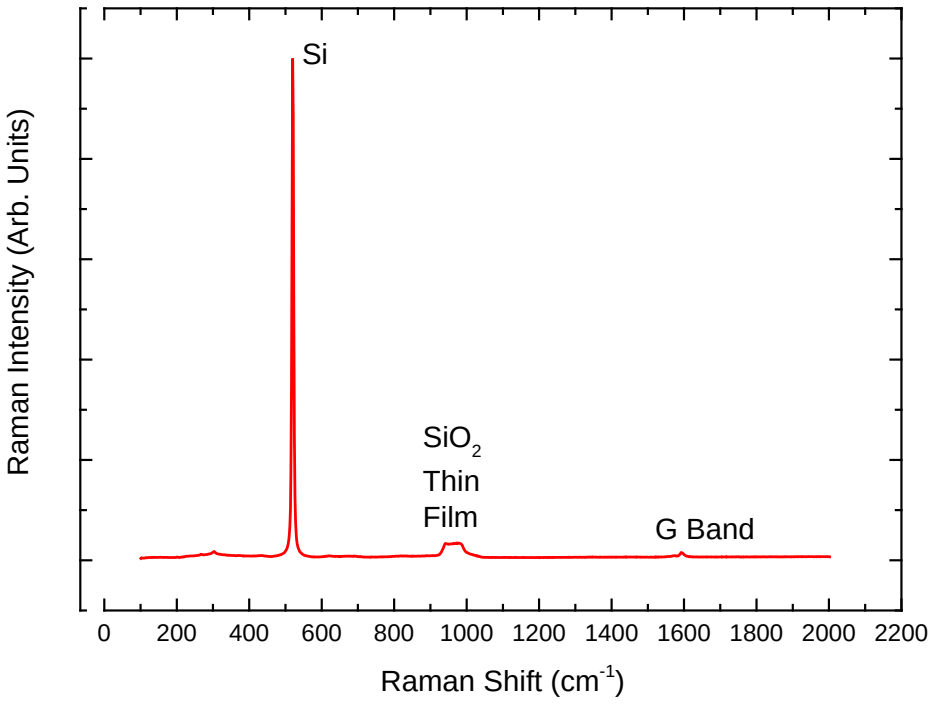

Figure 26: Representative Raman spectrum for the semiconducting SWCNT transistor EKS01 prior to irradiation.

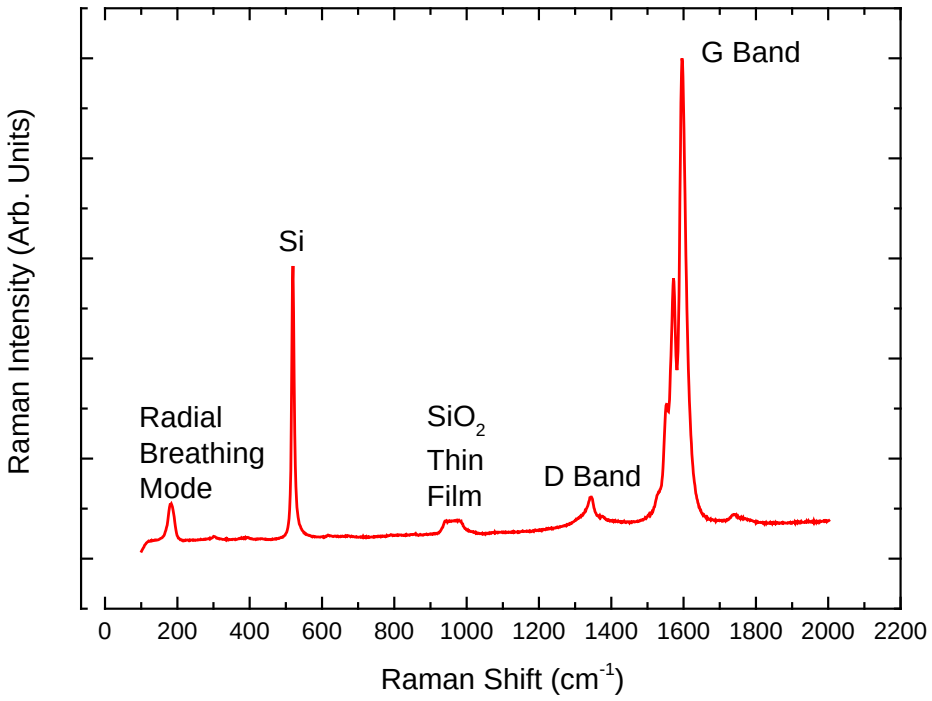

Figure 27: Representative Raman measurement for the semiconducting/metallic SWCNT transistor EKSM01 prior to irradiation.

Pre-irradiation Raman spectra were taken the week prior to proton irradiations. A random sampling of 10 measurements was taken across the 6 EKS01 reticles and 6 EKSM01 reticles that would be irradiated, and all measurements were taken in the channel region. Following irradiation as outlined above, 5 Raman spectra were taken on every irradiated reticle, resulting in a total of 30 Raman spectra across the 6 reticles.

3.2.5 Proton Irradiation

After the pre-irradiation characterization of all reticles, samples were transported to the Pelletron facility for 1.8 MeV proton irradiation. The Pelletron electrostatic particle accelerator utilized for proton irradiation of the transistors is located at the Institute of Space Defense and Electronics (ISDE) on the Vanderbilt University campus. The accelerator was designed and manufactured by the National Electrostatic Corporation with a positive radio frequency (RF) ion source capable of producing up to 4 MeV H^+, 6 MeV He^+, or 14.3 MeV O^+ ions. For the purpose of these irradiations, only the 1.8 MeV H^+ source was used.

A total of 12 reticles, 6 reticles from each device type, were irradiated at 3 different fluences: 1×10^{12}, 1×10^{13} and 2×10^{13} protons/cm^2; the total ion fluence was determined by the ISDE staff using a current integrator. Proton fluences were selected based on the NIEL damage in silicon equivalent to previous electron irradiation studies at 1×10^{16} and 1×10^{17} electrons/cm^2 [3], [10]. During irradiations, the nominal flux of protons was 1×10^{9} protons/cm^{2}sec, which resulted in irradiation times of 16.67 minutes, 2.77 hours and 5.55 hours, respectively, to reach the fluences listed above. For all irradiations, the individual reticles were mounted to a stainless steel back plate using silver paint, as shown in Figure 28. The back plate was then attached to the assembly on

the sample mounting plate in the chamber, as shown in Figure 29. After all samples were mounted, the chamber was evacuated.

Following irradiation, all samples were removed from the back plate using acetone to remove all the silver paint, followed by an ethanol wash to remove all impurities that the acetone would leave behind on the reticles. After this cleaning process, the samples were allowed to sit and dry in air prior to characterization.

The stage used to mount the samples was grounded to the beam chamber, and allowed for multi-sample mounting due to its ability to rotate about the x- and z-axes, while allowing for minimal translation in the y-axis. In this way, multiple samples could be rotated into the beam line without breaking the vacuum seal, as depicted in Figure 30. Due to the horizontal orientation of the sample mounting stage, all samples were required to be mounted vertically using stainless steel plates to place samples into the beam line.

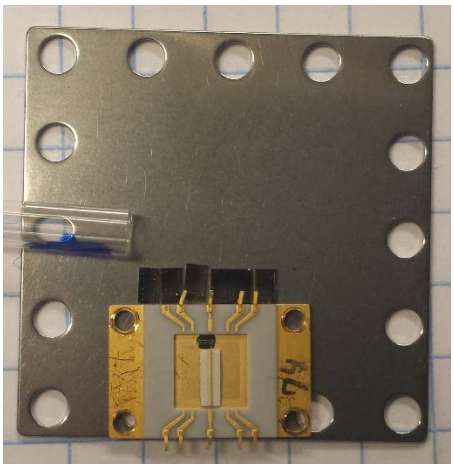

Figure 28: The arrangement of sample reticles, along with several ride-along samples for other projects mounted on the steel back plate that was used as a charge sink during irradiations, and to fix the samples in the beam line.

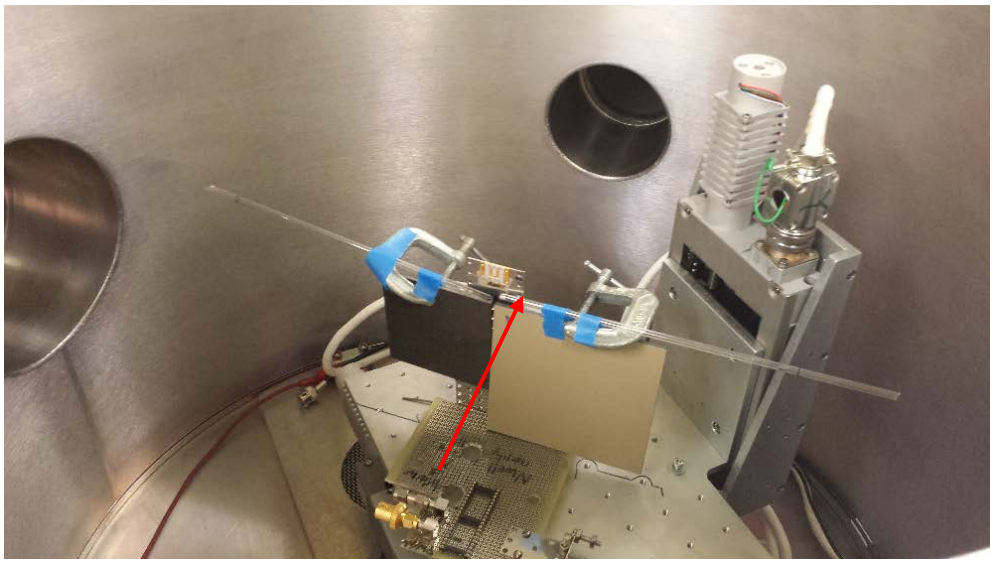

Figure 29: Vertically mounted samples in the sample chamber, with several ride-along samples. The sample mount is aligned with the beam line and the dosimetry equipment can be seen attached to the sample stage. The arrow shows the direction of the beam line.

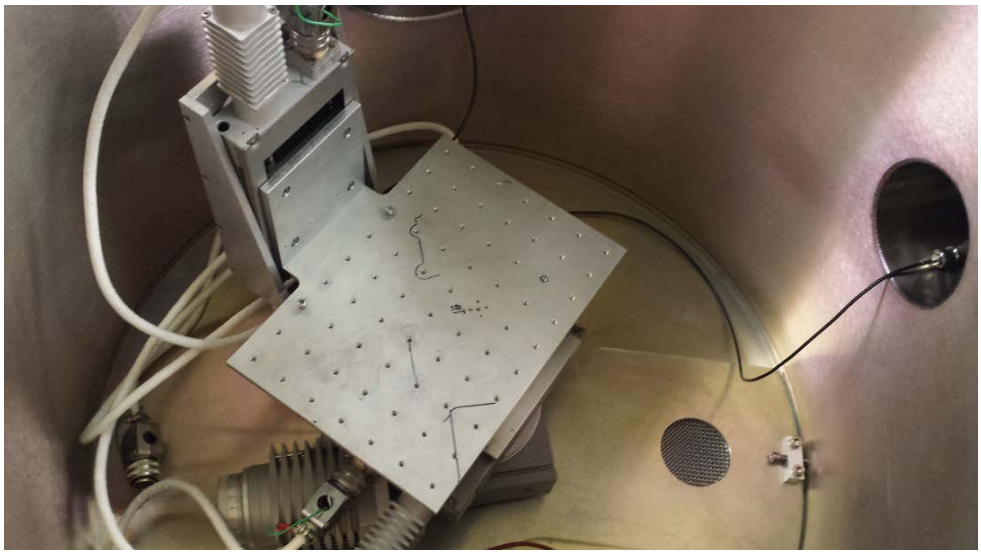

Figure 30: The sample mounting stage showing the horizontal orientation of the stage required for vertical sample mounting.

IV. Results and Analysis

4.1 Raman Study

The Raman spectroscopic study provided a method to isolate the radiation damage to the individual SWCNTs from other damage effects on the device level. Depending on density of the SWCNT network across the gate area of the transistors, the results showed some correlation between the total proton fluence and an increase in the *D* band peak relative to the intensity of the *G* peak, in the normalized spectra. The results weakly correlated with the results observed by Rossi *et al.* [6] for ions and Francis *et al.* [3] and Best *et al.* [10], for the electron irradiations described in Chapter II. The results served as an important factor in determining the radiation damage in the SWCNT networks by quantification of the *D/G* peak ratios as a function of proton fluence. These results were compared to the transistors current-voltage properties, as well as the charge pumping current, which were used to characterize radiation-induced changes in the oxide layer.

4.1.1 Semiconducting SWCNT Transistors

The semiconducting SWCNT transistor reticles were characterized by Raman spectroscopy measurements prior to and following irradiation, as outlined in Chapter III. While the characteristic peaks for SWCNTs were observed at 1340-1345 cm^{-1} and 1590-1595 cm^{-1}, the intensity of the Si and SiO_2 peaks overwhelmed the Raman vibrational modes for the SWCNTs. From previous measurements, it was determined that the SWCNT networks dispersed across the gate area were of a low-density, and non-

uniformly distributed. Even utilizing 100% laser power on the Raman spectroscopy system, the intensity of the *G* peak was on the order of 1% of the characteristic silicon peak intensity, leading to a small signal to noise ratio in the observed *D/G* peaks. This signal-to-noise ratio with respect to the minute *D* peak intensity is clearly observable in Figures 31 and 32, which shows the Raman spectra of the *D* and *G* peaks before and after irradiation to fluences of 10^{12}, 10^{13}, and 2×10^{13} protons/cm^2. Table 1 lists the measured *D/G* ratios observed before and following irradiation, along with the standard deviations, for the semiconducting samples.

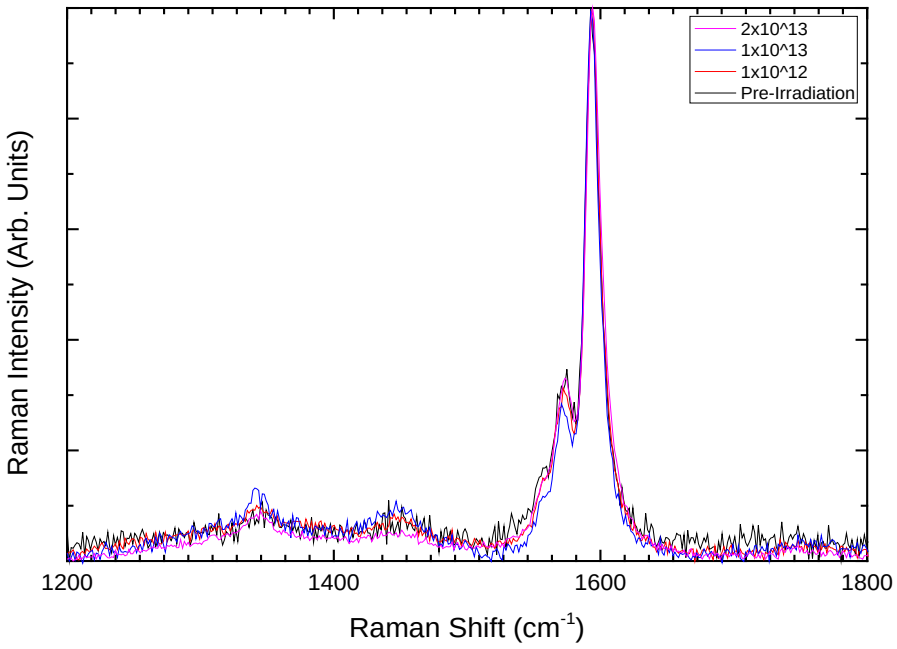

Figure 31: Normalized Raman spectra for EKS01, the semiconducting SWCNT transistor sample, before and after irradiation to fluences of 10^{12}, 10^{13}, and 2×10^{13} protons/cm^2. Spectra are normalized to the magnitude of the *G* peak. The *D* peak is barely observable above the noise and background of the Raman measurement.

Following irradiation, there was minimal dependence of the *D/G* ratios as a function of the proton fluence. Nominally, the *D/G* ratio remains fairly constant,

indicating little radiation-induced damage in the SWCNTs, likely due to the low density of SWCNTs across the gate area decreasing the overall probability of a knock-on effect displacing a carbon atom from the CNT lattice.

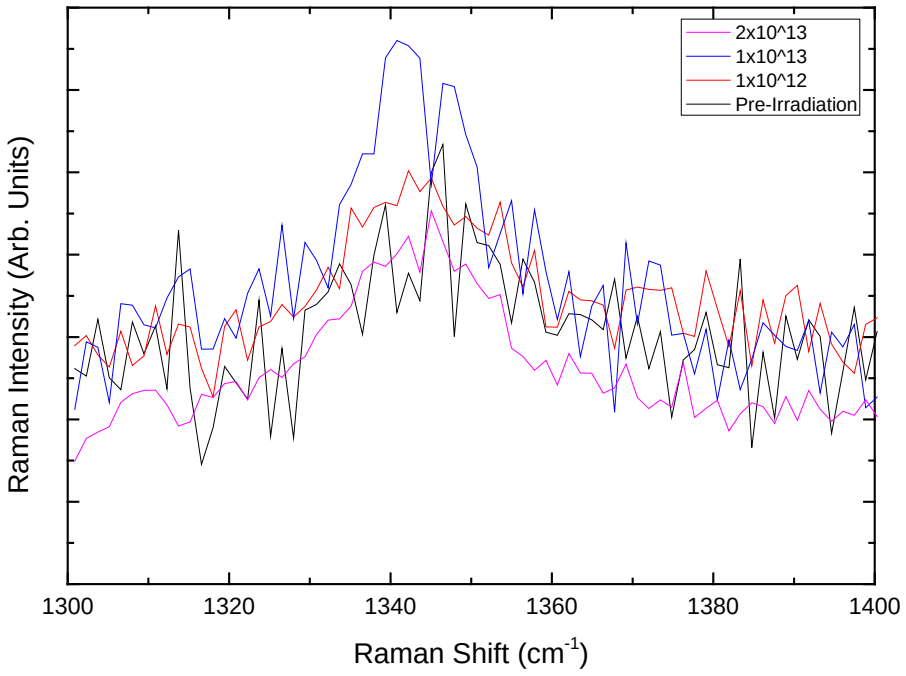

Figure 32: The measured *D* peak for the semiconducting sample, before and after irradiation to fluences of 10^{12}, 10^{13}, and 2×10^{13} protons/cm^2. Spectra shows the significant amount of noise observed due to the low density of SWCNTs across the gate area. The spectra show that the intensity of the *D* peak does not increase or change significantly as a function of proton flux for this low density dispersion of SWCNTs across the gate.

Table 1: The *D/G* ratios for EKS01, the semiconducting SWCNT transistor sample, before and after proton irradiation. The fluences are presented, with all irradiations performed using 1.8 MeV protons.

EKS01	SEMICONDUCTING	
FLUENCE (cm^{-2})	***D/G* Ratio**	**Std. Dev**
PRE	0.107	0.099
1×10^{12}	0.100	0.057
1×10^{13}	0.132	0.049
2×10^{13}	0.091	0.083

As shown in Table 1, irradiation to a fluence of 1×10^{13} protons/cm^2 introduced relatively more radiation damage to the SWCNT networks than the higher fluence of 2×10^{13} protons/cm^2, which is counter intuitive. An increase in the *D/G* ratio would indicate a higher percentage of vacancies and broken bonds within the SWCNTs, which are all symmetry breaking defects in the nanotubes. However, a collection of defects in a single spot that shears the nanotube would not appear through Raman spectroscopy since the symmetry about the sp^2 bonds in the graphene sheet is not broken. Increasing proton fluence could result in more severed nanotubes, though the samples themselves could be actively annealed during irradiation due to internal heating. The only thermal conduction path from the samples in the beam line was the stainless steel back plate, which had no assisted cooling to maintain a constant temperature. No temperature measurements were taken, but heating could occur due to the energy deposited into the substrate during the proton irradiation. Localized heating of the substrate could potentially have an annealing effect, improving the *D/G* ratio by annealing out intrinsic defects.

4.1.2 Semiconducting/Metallic SWCNT Transistors

Semiconducting/metallic SWCNT transistors were irradiated simultaneously semiconducting with the SWCNT transistors, so that any parallels could be observed between the two samples. The observed spectra in Figure 33 were as expected for a film of SWCNTs, with the intensity of the *G* band significantly higher than that of the Si and SiO_2 peaks. The density of SWCNTs across the gate area in all semiconducting/metallic SWCNT transistors was much higher than that of the semiconducting SWCNT transistors. Table 2 shows the results of the irradiation study.

The signal-to-noise ratio is significantly higher through simple observation in Figures 33 and 34 relative to the lower density semiconducting SWCNT transistors, along with a much smaller standard deviation between individual measurements. The *D/G* ratio increases by 34% after irradiation to a proton fluence of 1×10^{12} protons/cm^2, and increases further to 66% above the pre-irradiation value at 1×10^{13} protons/cm^2, consistent with what was observed in the semiconducting SWCNT samples. After a fluence of 2×10^{12} protons/cm^2, the *D/G* ratio decreases, which is consistent with the trend observed previously in the semiconducting SWCNT transistors. This reproducibility, regardless of the type and density of the SWCNT network, aids in supporting the claim that the effect observed is likely *in-situ* radiation annealing. A similar effect was observed in previous studies utilizing electron irradiations at a constant energy, where the *D/G* ratio decreased at a higher electron fluence [10].

Table 2: The *D/G* ratios for EKSM01, the semiconducting/metallic SWCNT transistor sample, before and after proton irradiation. The fluences are presented with all irradiations performed using 1.8 MeV protons. Values show an increase in the *D/G* ratio due to radiation, however the apparent trend increases up to 1×10^{13} protons. However, the same trend does not continue for irradiations up to 2×10^{13} protons/cm^2.

EKSM01	SEMICONDUCTING/METALLIC	
FLUENCE (cm^{-2})	***D/G* Ratio**	**Std Dev**
PRE	0.067	0.0032
1×10^{12}	0.090	0.0016
1×10^{13}	0.111	0.0015
2×10^{13}	0.078	0.0026

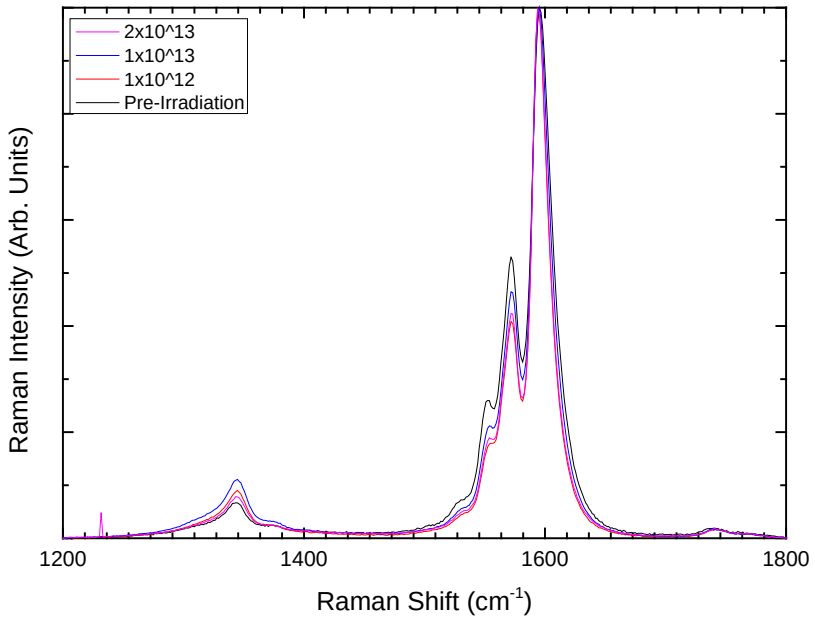

Figure 33: Normalized Raman spectra for EKSM01, the semiconducting/metallic SWCNT transistor sample, before and after irradiation to fluences of 10^{12}, 10^{13}, and 2×10^{13} protons/cm^2. Spectra are normalized to the magnitude of the *G* peak.

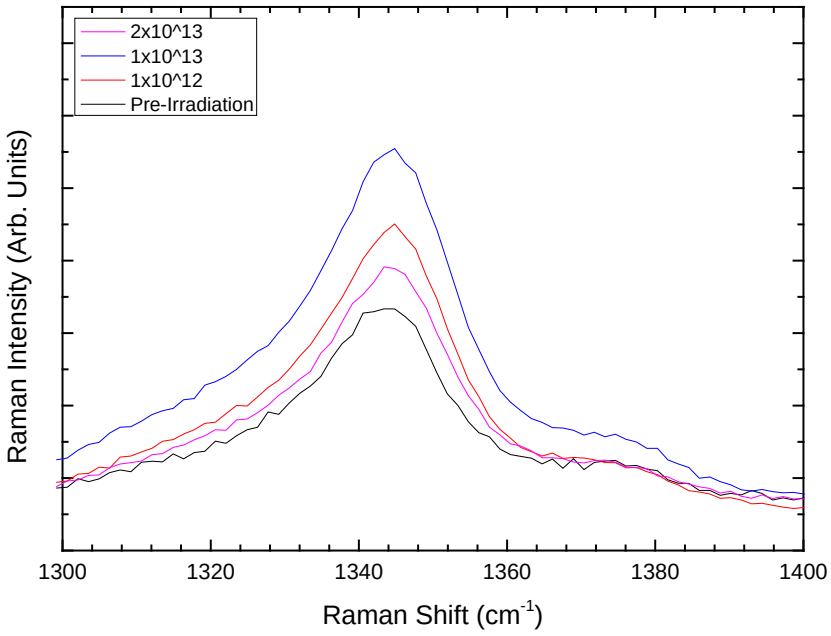

Figure 34: Raman spectra specifically showing the *D* peak observed in EKSM01 as a function of proton fluence. An increase is observed due to proton irradiation; however, a clear trend as a function of the fluence is not observed.

4.2 Charge Pumping Study

The next phase of the experiment was to determine the radiation damage to the oxide through the use of charge pumping measurements from which interface trap densities can be estimated. The importance of characterizing the trap density is two-fold, since interface traps contribute both to the device hysteresis and the drain current observed in current-voltage measurements. Results for the semiconducting SWCNT transistors correlate to previous studies by Francis *et al.* [3]. It is assumed that the resulting recombination current in the charge pumping study is dominated by trapping at the SWCNT/SiO_2 interface. This assumption is not completely valid since atmospheric adsorbates on both SWCNT and oxide surfaces act as trap centers, also contributing to the measured recombination current. The non-uniformity of the SWCNT distribution across the gate channel from device to device and the variability in SWCNT density between devices adds to a likely underestimation of the recombination current [3]. Only the gate area covered by SWCNTs conducting current between the source and drain is measured through charge pumping. Since equation (1) requires the gate, a larger gate area will be assumed in comparison to the actual gate area measured. The higher density of SWCNTs in the semiconducting/metallic samples should minimize this underestimation of the recombination current relative to the semiconducting SWCNT transistor samples.

4.2.1 Semiconducting SWCNT Transistors

Charge pumping was completed on the same semiconducting reticles presented in the Raman spectroscopy study, both prior to and following irradiation. The large variability in the uniformity of SWCNTs across the gate area is clearly observable in

Figure 35, which shows the interface trap density as a function of the distance from the oxide interface and proton fluence. The error bars shown are the standard deviations across the transistors on the reticles tested at each fluence. These standard deviations are on the order of the mean value observed, which further supports the claim that there is significant non-uniformity in the SWCNT distribution across the gate area. The recombination current is the dominating factor in calculating the interface trap density. The only other factor that changes from transistor to transistor in the calculations is the threshold voltage, which is determined from the pre- and post-irradiation current-voltage characteristics. A change of 2 V in the threshold voltage only varies the calculated trap density by ~10%. The threshold voltage is used in equation (2) to estimate the energy range swept during charge pumping measurements

The general trend of the trap density profile can be observed in Figure 36, which shows the interface trap density as a function of distance from the SWCNT/oxide interface for the semiconducting SWCNT transistors, before and after irradiation to fluences of 10^{12}, 10^{13}, and 2×10^{13} protons/cm^2. The trap density profile is similar profile for all pre- and post-irradiation charge pumping calculations. A reduction in interface trap density following proton irradiation occurs, similar to what was observed in [3]. This reduction in recombination current is potentially due to an increase in the gate leakage current as a function of proton irradiation. However, since the transistors are unpassivated, the major contributor to interface trapping is likely adsorbates on the SiO_2 and SWCNT surfaces. Therefore, the measured recombination current is mostly from adsorbates; while it is possible that the radiation-induced SWCNT/SiO_2 interface traps are significant, the significance of the interface traps is not observed in the test setup.

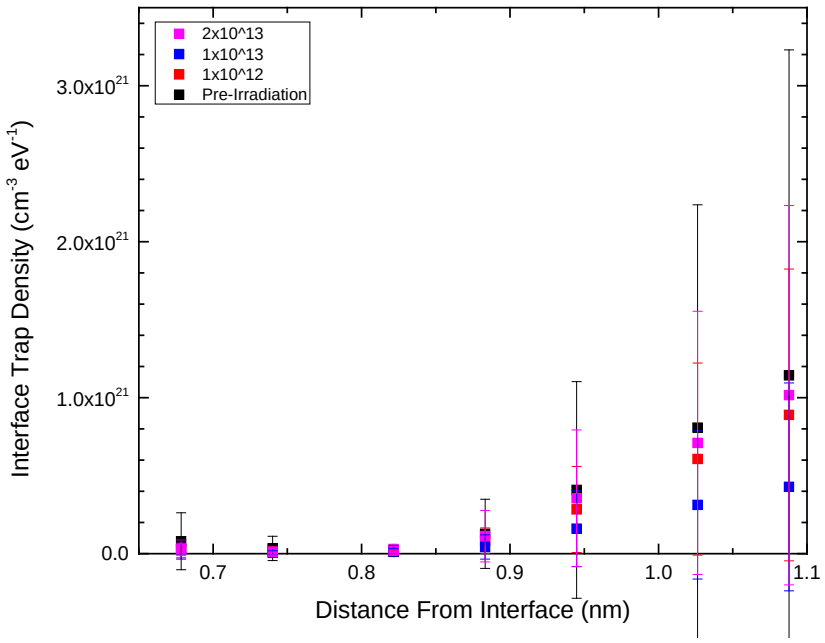

Figure 35: Interface trap density as a function of distance from the interface for EKS01 semiconducting SWCNT transistors, before and after irradiation to fluences of 10^{12}, 10^{13}, and 2×10^{13} protons/cm^2, plotted on a linear scale to highlight the error in the interface trap density calculated across all transistors on each reticle. The same interface trap profile is seen across all transistors, however no trend with proton fluence is observed.

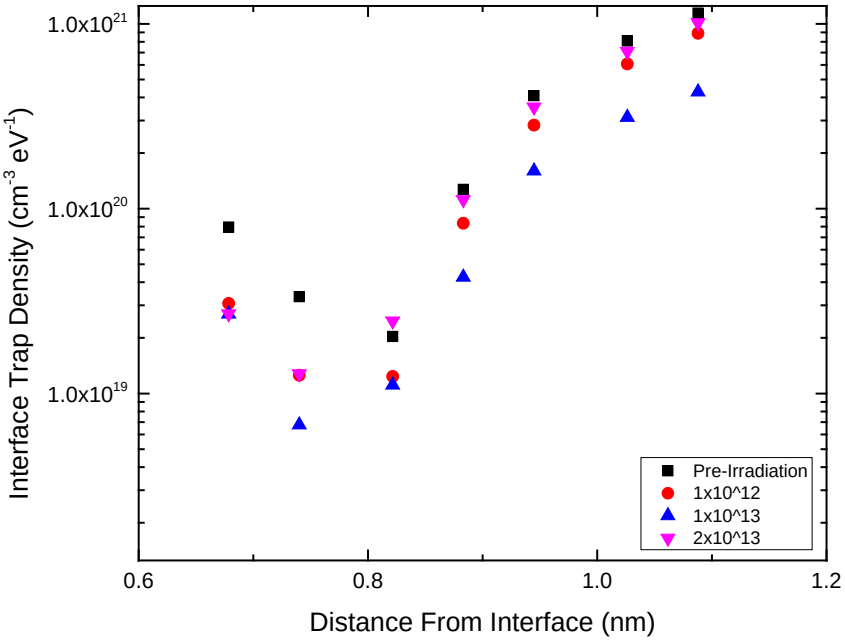

Figure 36: Interface trap density as a function of distance from the interface for EKS01 semiconducting SWCNT transistors, before and after irradiation to fluences of 10^{12}, 10^{13}, and 2×10^{13} protons/cm^2, plotted on a semi-log scale. A similar trend of trap densities is observed across all transistors. Calculated trap density is reduced post-irradiation relative to pre-irradiation.

Table 3 shows a summary of the calculated interface trap densities as a function of distance from the SWCNT/oxide interface, before and after irradiation to fluences of 10^{12}, 10^{13}, and 2×10^{13} protons/cm^2. Referring back to Figure 36, Table 3 shows that the change in interface trap density at each depth varies only by ~50% of the maximum calculated value, while the standard deviations observed in the figure exceed 100% of the maximum value calculated, so that only the extremes at each distance from the interface fall outside of the values calculated for every other fluence. Therefore, no significant trend is observed with fluence when the total error in the calculations is taken into account. Since Table 3 shows an interface trap density variation of ~2×10^{19} to 1×10^{21} cm^{-3}eV^{-1} and the nominal atomic density of silicon dioxide is known to be 2.3×10^{22} cm^{-3}, the trap density is on the order of 0.1% to 10% eV^{-1} of the SiO_2 at the interface.

Table 3: Interface trap density for EKS01 semiconducting transistor reticles before and after proton irradiation to fluences 1×10^{12}, 1×10^{13}, and 2×10^{13} protons/cm^2.

	EKS01	SEMICONDUCTING		
Z (nm)	**Pre-Irr. (cm^{-3}eV^{-1})**	**1×10^{12} (cm^{-3}eV^{-1})**	**1×10^{13} (cm^{-3}eV^{-1})**	**2×10^{13} (cm^{-3}eV^{-1})**
1.088	1.14×10^{21}	8.89×10^{20}	4.28×10^{20}	1.02×10^{21}
1.026	8.08×10^{20}	6.07×10^{20}	3.12×10^{20}	7.10×10^{20}
0.945	4.08×10^{20}	2.83×10^{20}	1.60×10^{20}	3.55×10^{20}
0.883	1.27×10^{20}	8.34×10^{19}	4.26×10^{19}	1.12×10^{20}
0.822	2.04×10^{19}	1.24×10^{19}	1.11×10^{19}	2.47×10^{19}
0.740	3.34×10^{19}	1.25×10^{19}	6.77×10^{18}	1.28×10^{19}
0.679	7.95×10^{19}	3.07×10^{19}	2.69×10^{19}	2.70×10^{19}

4.2.2 Semiconducting/Metallic SWCNT transistors

Charge pumping measurements were completed on the same samples studied in the Raman spectroscopy study pre- and post-irradiation. While the density of SWCNT

across the gate area is greater than that of the purely semiconducting samples, Figures 37 and 38 still shows a significant variation in the transistor-to-transistor recombination current, similar to what was observed in the semiconducting SWCNT transistors. Likewise, the similar trend of interface trap densities as a function of the distance from the interface is found for all fluences. However, in this case, an increase in the number of interface traps is observed, as shown in Table 4.

Table 4: Interface trap density for EKSM01 semiconducting/metallic transistor reticles before and after proton irradiation to fluences of 1×10^{12}, 1×10^{13}, and 2×10^{13} protons/cm^2. An apparent increase of interface traps at 1.09 nm as a function of fluence is observed.

	EKSM01	SEMICONDUCTING/METALLIC		
Z (nm)	**Pre-Irr. ($cm^{-3}eV^{-1}$)**	**1×10^{12} ($cm^{-3}eV^{-1}$)**	**1×10^{13} ($cm^{-3}eV^{-1}$)**	**2×10^{13} ($cm^{-3}eV^{-1}$)**
1.088	1.25×10^{22}	2.33×10^{22}	2.32×10^{22}	4.15×10^{22}
1.026	7.95×10^{21}	1.25×10^{22}	1.78×10^{22}	1.68×10^{22}
0.945	8.02×10^{21}	1.02×10^{22}	2.43×10^{22}	1.02×10^{22}
0.883	5.07×10^{21}	4.04×10^{21}	1.45×10^{22}	3.49×10^{21}
0.822	2.72×10^{21}	6.76×10^{20}	3.09×10^{21}	6.09×10^{20}
0.740	9.56×10^{20}	4.21×10^{20}	1.18×10^{21}	3.89×10^{20}
0.679	2.21×10^{21}	2.07×10^{21}	3.99×10^{21}	1.85×10^{21}

At a depth of 1.09 nm from the surface, there is a clearly observable increase in the interface trap density as a function of proton fluence. However, the values calculated exceed the atomic density of SiO_2. Overall, the trap densities vary from 10% to 200% of the atomic density of SiO_2, which indicates that atmospheric adsorbates contribute significantly to the estimated interface trap density. With a higher density of SWCNTs across the gate area, there is more CNT surface area for water molecules and gasses to adsorb to, which would lead to an increase in the measured recombination current, and thus the calculated interface trap density.

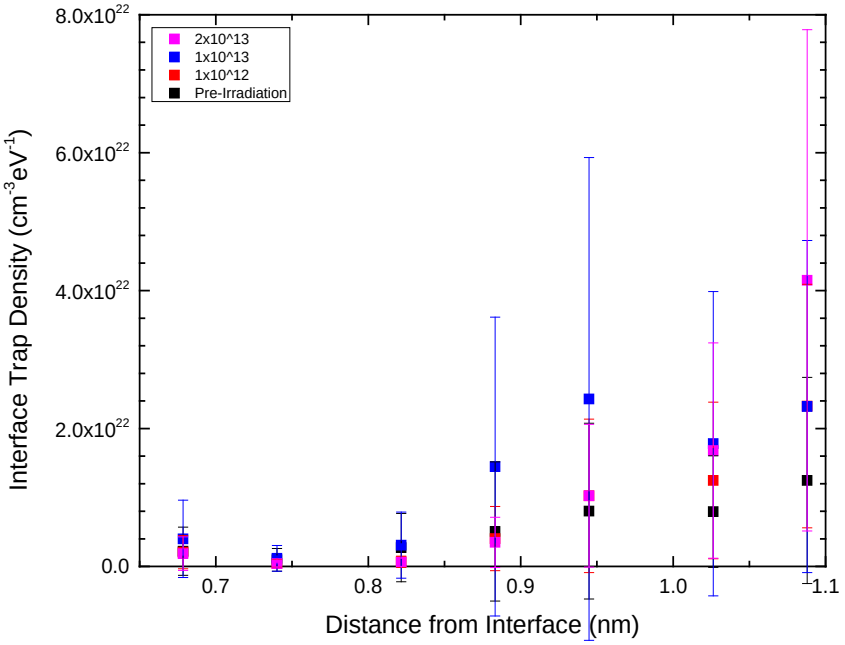

Figure 37: Interface trap density as a function of distance from the interface for the EKSM01 semiconducting/metallic SWCNT transistors, before and after irradiation to fluences of 10^{12}, 10^{13}, and 2×10^{13} protons/cm^2, plotted on a linear scale to highlight the error in the interface trap densities calculated across all transistors on each reticle.

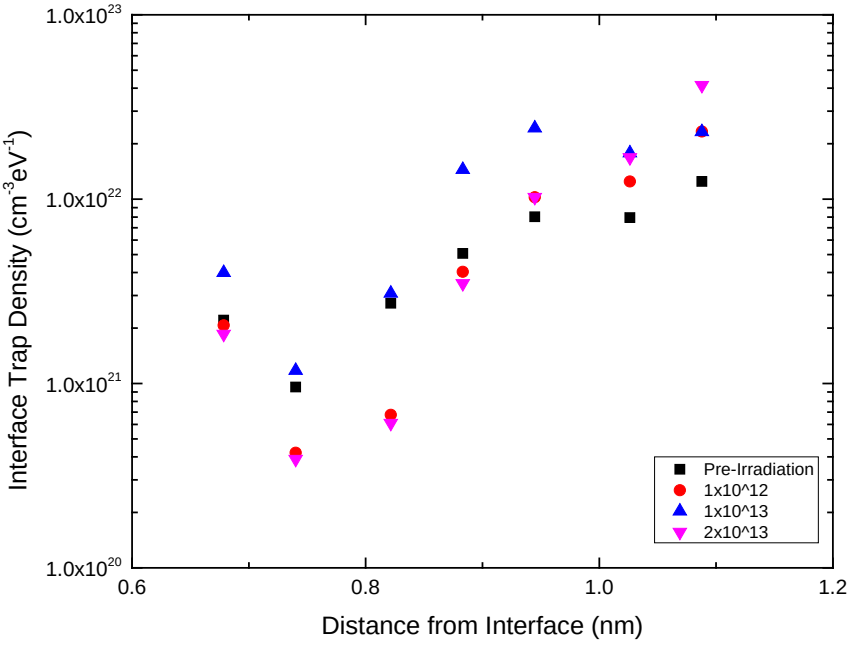

Figure 38: Interface trap density as a function of distance from the interface for the EKSM01 semiconducting/metallic SWCNT transistors, before and after irradiation to fluences of 10^{12}, 10^{13}, and 2×10^{13} protons/cm^2, plotted on a semi-log scale.

The standing hypothesis for both semiconducting and semiconducting/metallic SWCNT transistors is surface adsorbates dominate the calculated interface trap densities, while the non-uniform distribution of the SWCNTs across the gate area further adds to the error in calculations.

4.3 Current-Voltage Characterization Study

The previous Raman and charge pumping studies were used to aid in analyzing and correlating the radiation damage observed in the SWCNTs and substrate to the effects observed on transistor functionality as a whole. Both semiconducting and semiconducting/metallic transistors were measured prior to and following irradiation to determine the changes in transistor properties as a function of the total proton fluence.

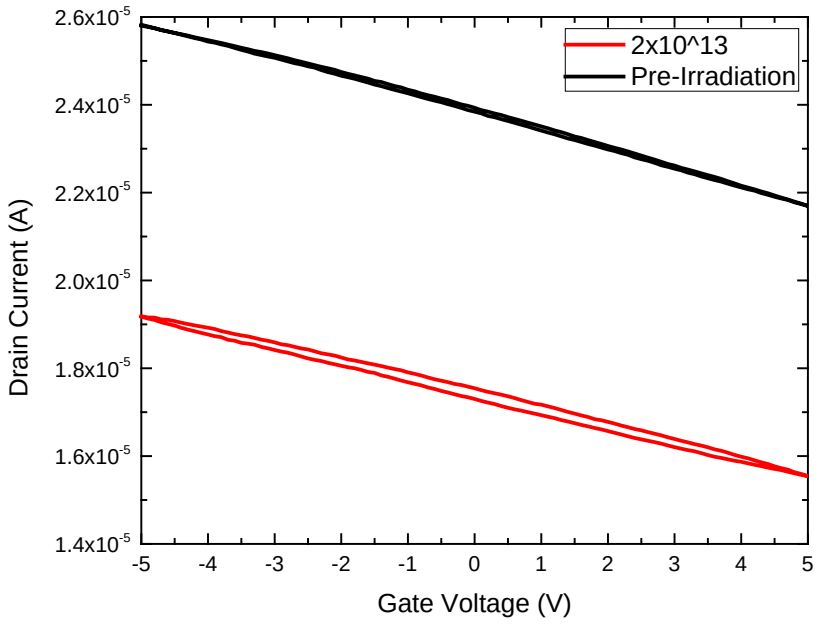

Figure 39: Drain current as a function of gate voltage for semiconducting/metallic SWCNT transistors EKSM01 before and after irradiation to a fluence of 2×10^{13} protons/cm^2. Drain current shows the poor on/off characteristics with a hysteresis of 0.1 V before proton irradiation and 0.5 V after.

As outlined in Chapter III, all semiconducting SWCNT transistors were characterized to determine the threshold voltage shift, change in drain current, change in hysteresis, and change in gate current leakage as a function of irradiation. The semiconducting/metallic SWCNT transistors showed no on/off characteristic, and exhibit a drain current that is linear with gate voltage, as illustrated in Figure 39.

Results observed in the semiconducting devices correlate to previous studies on SWCNT transistors exposed to electron irradiations [3], and gamma irradiations [5]. Effects observed in previous studies were due to ionizing radiation depositing charge into the gate oxide and formation of interface traps at the semiconductor/gate oxide interface.

4.3.1 Semiconducting SWCNT Transistors

The semiconducting SWCNT transistors were characterized by current-voltage measurements as described in Chapter III. Device-to-device performance varied greatly and due to the low density of SWCNTs across the gate area, only transistors with gate lengths of 2 and 4 μm were functional. Transistors exhibited a variety of on/off ratios ranging from half an order of magnitude to 10^3, where the off-state of the device dropped into the thermal noise of the instrumentation ($<1\times10^{-15}$ A at the drain with a gate leakage current exceeding the measured drain current).

The threshold voltage was determined as outline in Chapter III, utilizing the linear region of the *I-V* curve with the drain current at the on-state of the reverse sweep from a gate voltage of +5 to -5V. The results of the threshold voltage analysis using the *I-V* curves are presented in Table 5. The threshold voltage shift is averaged across each reticle and presented with the standard deviation to show the variation across all

functioning devices. A negative shift in the threshold voltage can be explained by positive charge build up in the gate oxide, in which there is a buildup of low mobility holes. The holes in the oxide act as positive charge that requires a larger negative bias on the gate to switch the transistor into the on state. A depiction of the location of the charge build up can be observed in Figure 40.

Table 5: The threshold voltage shift in EKS01 semiconducting SWCNT transistors following irradiation to fluences of 1×10^{12}, 1×10^{13}, and 2×10^{13} protons/cm^2. While the standard deviation is significant, an apparent trend can be observed as the threshold voltage shift increases with increasing proton fluence.

EKS01 SEMICONDUCTING			
FLUENCE (cm^{-2})	**Sample**	**Threshold Voltage Shift (V)**	**Std Dev**
1×10^{12}	C3R10	-1.243	0.761
	C4R9	-1.360	0.650
1×10^{13}	C3R11	-1.400	0.562
	C5R9	-1.513	1.008
2×10^{13}	C2R9	-1.917	0.796
	C3R7	-1.911	0.804

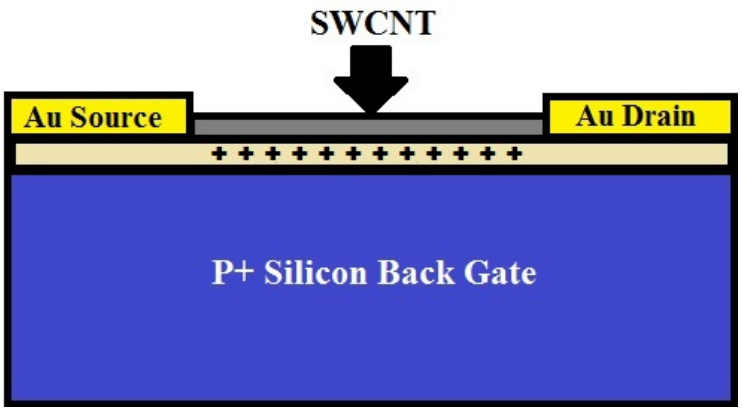

Figure 40: Diagram depicting the location of charge deposition in the gate oxide due to continuous proton irradiation.

Figure 41 shows a clear trend of increasing threshold voltage shift with an increasing proton fluence, indicating positive charge buildup in the oxide. This positive charge could exist due to several possible mechanisms. The first mechanism involves the generation of electron-hole pairs due to ionizing radiation from incident protons. Since the mobility of electrons is greater than the mobility of holes in SiO_2, the electrons are swept away in the presence of an electric field before recombination can take place, leaving a surplus of holes in the oxide. The second potential mechanism would be the release of hydrogen ions as protons, which can migrate to the interface under a positive gate bias. Both mechanisms could result in trapped positive charge and would potentially be fluence dependent.

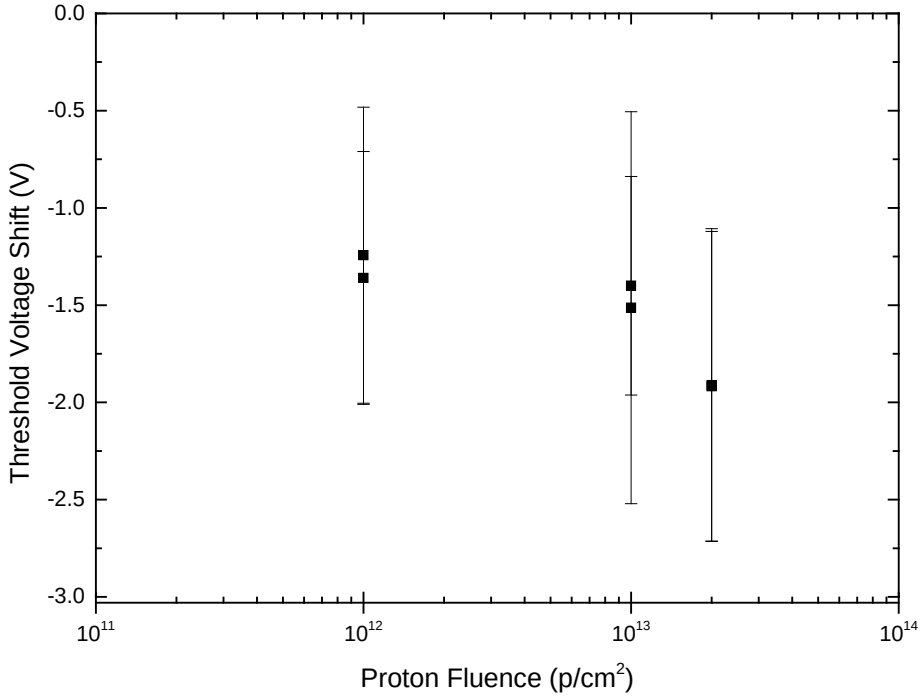

Figure 41: Threshold voltage shift as a function of proton fluence illustrating the increasing negative shift in the threshold voltage with increasing proton fluence for EKS01 semiconducting SWCNT transistors following proton irradiation.

After exposure to a proton fluence of 1×10^{12} protons/cm^2, an average threshold voltage shift of -1.30 V is observed averaged over the two irradiated reticles, which shifts an average of an additional -0.15 V after 1×10^{13} protons/cm^2. A maximum threshold voltage shift of -1.91 V occurs after a total fluence of 2×10^{13} protons/cm^2, which is a 32% increase in threshold voltage shift from the previous fluence. The trend follows the expected results of increasing proton radiation damage to the substrate, since minimal damage to the SWCNT network was observed in the Raman study.

The relative downshift or decrease in drain current was determined through a comparison of the drain current at 50% of the on-state prior to and following irradiation, as described in Chapter III. This drain current reduction is due to a combination of two mechanisms. The first mechanism is direct knock on damage to the SWCNTs by the proton irradiation causing vacancies and broken bonds in the individual CNTs, and leads to a decrease in the carrier mobility. The second mechanism is due to trapped charge in the oxide, which was confirmed by the existence of a threshold voltage shift. Trapped charge in the oxide causes a reduction in carrier mobility, having the greatest effect near the SWCNT/SiO_2 surface. Charge pumping was implemented to measure the trap density at the interface; however, the presence of adsorbates removed this technique as a viable way to verify the trap density.

The calculated relative downshifts are shown in Table 6, which shows a clear increase in the relative downshift as a function of increasing proton fluence. This increase in the relative downshift correlates well with the increase in the threshold voltage shift observed previously. Between 1×10^{12} and 1×10^{13} protons/cm^2 the relative downshift in drain current increases by 26%, which is larger than the 11% increase in the threshold

voltage shift between these two fluences. The difference in relative downshift after a fluence of 2×10^{13} protons/cm^2 is 38%, which correlates closer to the 32% increase in the threshold voltage shift.

Table 6: Table of the calculated downshift, or reduction in drain current relative to the initial drain current at the 50% level of the on/off point, before and after proton irradiation. Values show an increasing downshift with increasing proton fluence, which correlates to an increasing reduction in drain current. Presented values are an average across all transistors on a single reticle.

	EKS01 SEMICONDUCTING		
FLUENCE (cm^{-2})	**Sample**	**Relative Downshift**	**Std Dev**
1×10^{12}	C3R10	0.341	0.263
	C4R9	0.327	0.247
1×10^{13}	C3R11	0.391	0.264
	C5R9	0.453	0.172
2×10^{13}	C2R9	0.537	0.321
	C3R7	0.626	0.171

Transistor hysteresis was calculated as described in Chapter III. The cause of transistor hysteresis as observed in all transistors, is due to carrier trapping at trap sites originating from adsorbed gas and water molecules on the SWCNTs and oxide interface, and at interface and oxide traps in the SiO_2 layer. The hysteresis should correlate with the charge pumping calculations since the observed hysteresis is dependent on the interface trap density. The measured hysteresis is shown in Table 7 for the semiconducting SWCNT transistors before and after proton irradiation. Similar to the estimates from the charge pumping measurements, there is a significant standard deviation observed in the relative change between the hysteresis before and after irradiation. The largest hysteresis voltage is observed nearest to the on and off states, though the standard deviation is also the most significant at these locations, which indicates that the current-voltage

characteristics are least stable near the on and off state. This is why the 50% point is used as a standard for determining the relative downshift in drain current. A weak trend is observable at the 50% on/off state, which shows an increase in hysteresis with increasing proton fluence. However, the standard deviation is still significant.

Table 7: The relative change in the measured transistor hysteresis for EKS01 semiconducting SWCNT transistors before and after proton irradiation. The hysteresis is presented at three selected states to show the variability across each transistor and the instability of transistor properties near the on and off state.

EKS01 SEMICONDUCTING						
FLUENCE (cm^{-2})	**1×10^{12}**		**1×10^{13}**		**2×10^{13}**	
	Relative Change	**Std Dev**	**Relative Change**	**Std Dev**	**Relative Change**	**Std Dev**
5% FROM ON STATE	0.488	1.536	0.963	0.748	2.210	3.505
50%	0.073	0.481	0.072	0.406	0.173	0.450
5% FROM OFF STATE	0.740	2.134	0.354	0.267	0.618	0.831

The gate leakage current was analyzed using the method described in Chapter III. Leakage current through the gate during transistor operation is caused by tunneling through the gate oxide. Radiation is capable of increasing the gate leakage current through increased damage and trap sites that are created in the oxide in addition to the traps that already exist. Figure 42 shows the gate leakage current as a function of the gate voltage. No clear trend in gate leakage current is observable as a function of the proton fluence. A decrease in gate leakage current is actually observed following proton irradiation. Since the decrease is actually very consistent, as shown in Table 8, this suggests that the change in gate leakage current is a result of the contact resistance between the back gate of the reticle to the base plate on the probe station or radiation induced damage that increases the resistance through the back gate. The applied voltage

is a constant, and based on ohm's law ($V=IR$) a decrease in current relates directly to an increase in the resistance.

Table 8: The average gate leakage current at each proton fluence along with the change in current relative to the pre-irradiation measurements for EKS01 semiconducting SWCNT transistors following 1.8 MeV proton irradiation. The standard deviation is presented as a measure of the device to device consistency in the gate leakage current. A nearly constant relative decrease can be observed.

	EKS01	SEMICONDUCTING	
FLUENCE (cm^{-2})	**Gate Current Leakage (A)**	**Std Dev**	**Δ**
PRE	1.463×10^{10}	1.481×10^{10}	-
1×10^{12}	5.379×10^{11}	3.663×10^{11}	-6.323×10^{1}
1×10^{13}	6.093×10^{11}	9.420×10^{11}	-5.835×10^{1}
2×10^{13}	5.113×10^{11}	4.695×10^{11}	-6.505×10^{1}

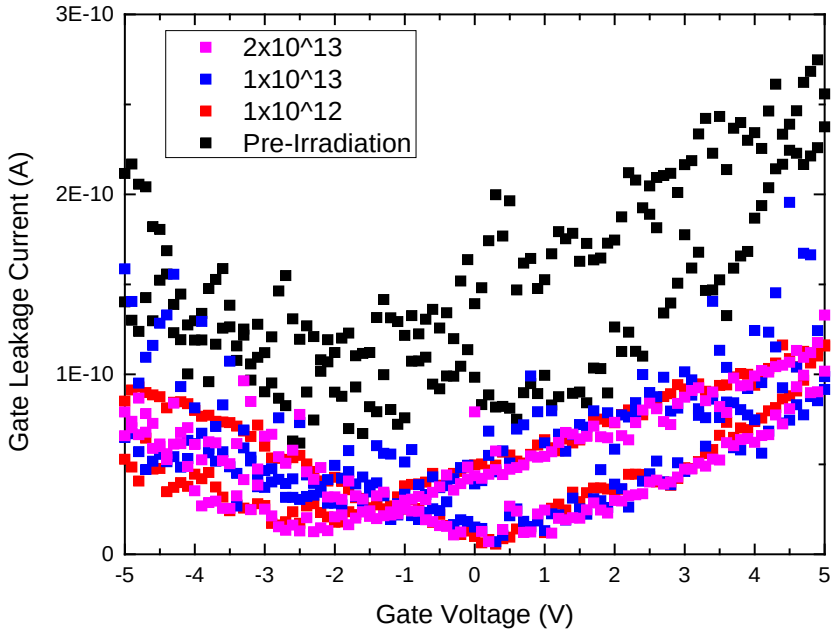

Figure 42: The average gate leakage current across all reticles of EKS01 at each proton fluence as a function of the gate voltage. There is no observable increase in the gate leakage current due to increasing proton fluence, instead a uniform decrease is observed at all proton fluences.

4.3.2 Semiconducting/Metallic Transistors

The semiconducting/metallic SWCNT transistors were characterized by current-voltage measurements as described in Chapter III. Device-to-device performance was observed to be very consistent, with the drain current scaling with gate area, similar to what is observed in conventional MOS devices. Their performance as transistors is poor since the semiconductor/metallic SWCNT mixture functions more as a resistor than a semiconducting material, resulting in current-voltage characteristics that are nearly linear, with no observable on/off states.

The same method previously described for the semiconducting SWCNT transistors was used to analyze the pre- and post-irradiation shift in the drain current for these semiconducting/metallic transistors. The calculated relative downshift before and after proton irradiation is presented in Table 9. Although there is an increase in the *D/G* ratio observed in the Raman study and an increase in the interface rap density as a function of fluence for these devices, there is no clear trend in the relative downshift as a function of proton fluence, which is in contrast to what is observed in the Raman and charge pumping measurements.

Table 9: The measured downshift, or reduction in drain current relative to the initial drain current, before and after proton irradiation. A downshift is observed due to proton irradiation, however as the values make it apparent there is no function of fluence observed.

	EKSM01	SEMICONDUCTING/METALLIC	
FLUENCE (cm^{-2})	**Sample**	**Relative Downshift**	**Std Dev**
1×10^{12}	C3R10	0.442	0.208
	C4R9	0.226	0.100
1×10^{13}	C3R11	0.440	0.101
	C5R9	0.400	0.037
2×10^{13}	C2R9	0.465	0.095
	C3R7	0.317	0.070

Hysteresis is determined using the method previously outlined for the semiconducting transistors; but is altered to only use the 50% on/off state due to a combination of the variability observed in the semiconducting SWCNT transistors and the fact that no hysteresis is observed at the 5% points in the semiconducting/metallic SWCNT transistors. Table 10 shows the results of the hysteresis study on EKSM01. Measurements show an increase in the hysteresis observed as a function of the proton fluence, similar to that observed in EKS01, however the change in hysteresis is more consistent. This could be attributed to the consistency observed in all of these transistors. The increase in transistor hysteresis correlates well with the charge pumping study, which showed an increase in the overall interface trap density as a function of proton fluence.

Table 10: The relative change in the measured transistor hysteresis before and after irradiation for the EKSM01 semiconducting/metallic SWCNT transistors. The hysteresis is measured at the 50% level of the on/off state for all transistors. An increase in the relative change is observed as a function of the proton fluence.

	EKSM01		SEMICONDUCTING/METALLIC			
FLUENCE (cm^{-2})	**1×10^{12}**		**1×10^{13}**		**2×10^{13}**	
	Hysteresis	**Std Dev**	**Hysteresis**	**Std Dev**	**Hysteresis**	**Std Dev**
PRE-IRR.	0.290	0.062	0.224	0.066	0.280	0.201
POST-IRR.	0.372	0.242	0.428	0.117	0.607	0.264
Δ	0.307	0.836	1.007	0.664	1.483	1.110

Gate leakage current analysis was performed as stated previously. No increase in the gate current is observed as a function of increasing proton fluence, which can be observed in Figure 43 and Table 11. This contrasts to the results of both the charge pumping and hysteresis analysis, which suggests an increase in the oxide trap density with irradiation. The lack of an increase could be attributed to an increase in the contact

resistance between the gate and the back plate utilized to apply the gate voltage, which is similar to what was observed in the semiconducting SWCNT transistors.

Table 11: The average gate leakage current at each proton fluence along with the change relative to the pre-irradiation measurements for EKSM01 semiconducting/metallic SWCNT transistors. The standard deviation is presented as a measure of the device to device consistency of the gate leakage current. No trend in the relative decrease in gate leakage current is observed with increasing proton fluence.

	EKS01	SEMICONDUCTING/METALLIC	
FLUENCE (cm^{-2})	**Gate Leakage Current (A)**	**Std Dev**	**Δ**
PRE	7.915×10^{11}	1.026×10^{10}	-
1×10^{12}	5.428×10^{11}	4.335×10^{11}	-3.142×10^{1}
1×10^{13}	7.069×10^{11}	9.581×10^{11}	-1.069×10^{1}
2×10^{13}	5.152×10^{11}	3.538×10^{11}	-3.491×10^{1}

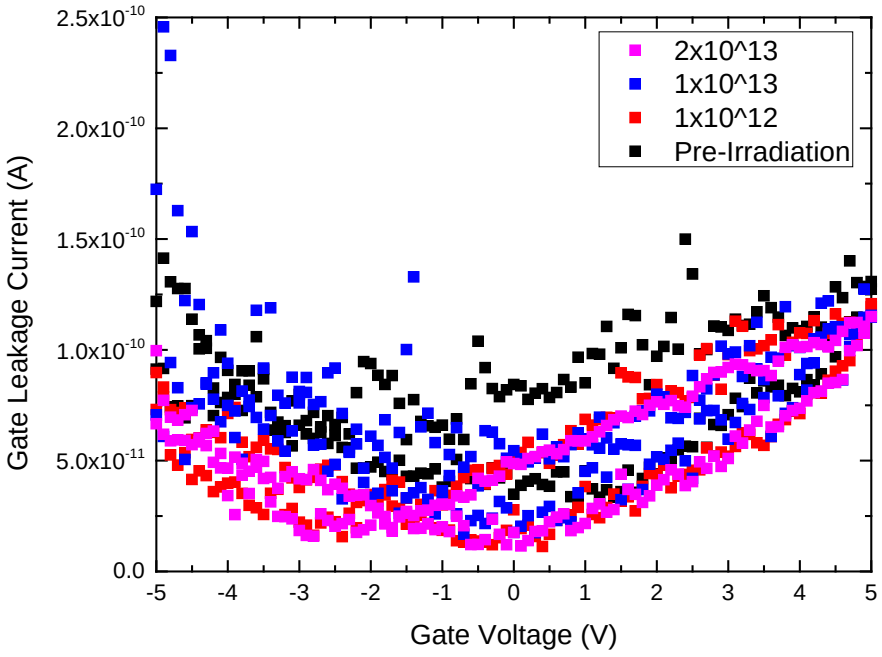

Figure 43: The average gate leakage current across all reticles of EKSM01 before and after proton irradiation. There is no observable increase in the gate leakage current due to increasing proton fluence. The gate current decreases slightly with the increasing proton fluence.

V. Conclusions

5.1 Raman Study

From Raman spectroscopy measurements on the semiconducting/metallic SWCNTs, an increase in the *D/G* ratio was observed after proton irradiation to a total fluence of 1×10^{12} protons/cm^2. However, after exposure to $2x10^{13}$ protons/cm^2, a decrease in *D/G* ratio was observed, likely due to annealing. Annealing was also observed in the lower-density network semiconducting SWCNT transistors following exposure to high proton fluences. However, much smaller changes in the *D/G* ratio with proton fluence were observed due to the low signal-to-noise ratio in the Raman spectroscopic measurements. The overall results show that the SWCNTs are radiation hardened up to around 1×10^{12} protons/cm^2 where only a 34% increase in the *D/G* ratio was observed in the higher density SWCNT network. The lower density SWCNT networks exhibited relatively little change in the *D/G* ratio, though there was significant standard deviation between the measurements.

5.2 Charge Pumping Study

The charge pumping study showed minimal trends in the interface trap density as a function of proton fluence. Significant error is introduced in the interface trap density calculations due to the contribution from atmospheric adsorbates to the total measured recombination current. Since all measurements are taken at ambient temperature and humidity, gases and water readily adsorb to the SWCNT and SiO_2 surfaces. A

combination of the adsorbates on the SWCNTs and SiO_2 surface, along with the significant device to device variation, in terms of both performance properties and SWCNT network distribution across the gate area, results in significant error in interface trap density estimations from charge pumping measurements. Charge pumping measurements performed on the higher density semiconducting/metallic SWCNT networks revealed an interface trap density that exceeded the atomic density of SiO_2. An excessive interface trap density is unrealistic and shows that the effect of the adsorbates is significant relative to the recombination current generated from traps in the SiO_2.

5.3 Current-Voltage Characterization

Current-voltage characteristics exhibited a decrease in the drain current as a function of the proton fluence for all SWCNT transistors. The possibility that this decrease in drain current is due to leakage through the gate was removed due to the fact that there was no significant increase in the gate leakage current as a function of the proton fluence for both transistors sets. Therefore, it can be concluded that the reduction in the drain current is due to the substrate charging observed as a significant threshold voltage shift as a function of the proton fluence. This charging in the oxide can locally shift the Fermi level in the SWCNT semiconductor such that the overall carrier density is reduced, reducing the drain current. At the 50% on/off point, a general increase in the hysteresis is observed as a function of proton fluence. This increase in hysteresis is due to an increase in charge trapping at trap sites located in the SiO_2 gate oxide, along with adsorbates on the SWCNT surface. Since the transistors were exposed to open air for 24+ hours, it can be assumed that the adsorbates had reached a similar saturation level seen

prior to irradiation under vacuum, where the adsorbates would desorb from the SWCNT surfaces. This results in the conclusion that the major factor in the increase in the observed hysteresis is due to the increase in observed interface traps in the gate oxide.

5.4 Future Work

This work should be repeated with a proton energy of 1.8 MeV, using single reticles that have been packaged and wire bonded, allowing for *in-situ* measurements of the individual transistors. Both current-voltage characterization and charge pumping could be performed at predetermined fluence steps to determine the change in the electrical properties as a function of proton fluence. Additionally, *in-situ* measurements and transistor packaging allow for all measurements to be completed under vacuum, removing the effects of adsorbates on the transistor hysteresis and interface trap densities. A further study into short term annealing effects versus long term annealing effects on the radiation induced damage would be possible with *in-situ* measurements. The experimental plan used in this study left 24+ hours prior to electrical characterization where most if not all short term annealing effects were ignored. Furthermore, a study involving 1.8 MeV proton fluences up to 10^{14} protons/cm^2 should be explored. Intentions existed for exposures up to this fluence; however, the proton beam at the time was not capable of producing the flux required to reach this total fluence within a reasonable amount of time.

Another possible study would be to explore passivation techniques of the exposed SWCNT surface based on current research into hydrophobic self-assembled monolayers. Passivation would increase the device-to-device consistency in air. To better understand

the radiation effects on this passivation layer the goal of these studies should be two fold, encompassing both device and thin films. Studying the radiation damage to a passivated thin film using Raman spectroscopy and Hall Effect measurements would allow for the isolation of the passivation layer and SWCNT radiation damage effects from the damage effects observed at the transistor level. Device design could be further improved through the use of more radiation hardened gate oxides, such as hafnium oxide or aluminum oxide, as opposed to silicon dioxide.

5.5 Overall Conclusions

Overall, this study compares well to previously published work on both electron, ion and alpha particle irradiations, adding to the continuously growing field of carbon-based devices. A consistent decrease in the device drain current and shift in the threshold voltage was observed for all devices under high proton fluences. As observed in this study, the majority of the radiation damage observed was due to substrate effects on the transistor performance, while SWCNT damage observed through Raman spectroscopy was a relatively minor factor.

Referring back to Chapter I, the most prevalent radiation environment where a transistor would experience radiation damage of significant fluence and energy in comparison to the high fluences observed in this study would be a satellite deployed into low-earth orbit. Based on the fluences observed in low-earth orbit, transistors would only be exposed to a nominal value of 6.4×10^{9} to 6.4×10^{10} protons/cm^{2} of 1.8 MeV protons. A several orders of magnitude increase in proton fluence from the nominal fluence observed in low-earth orbit is required to observe significant radiation damage to devices, though

this might not always hold true since enhanced low dose radiation sensitivity (ELDRS) could have significant effects on device performances over the expected 5-50 year lifetime of a satellite. Given the proper design considerations, SWCNT transistors show promise for space and other high radiation environments requiring electronics.

Bibliography

[1] Iijima S. “Helical microtubules of graphitic carbon,” *Nature*, 354:56-58 (Nov. 1991).

[2] Merkoci, A. “Carbon Nanotubes in Analytical Sciences,” *Microchim Acta*, 152:157-174 (2006).

[3] Francis S. A., Cress C. D., McClory J. W., Moore E. A., and Petrosky J. C. “Characterization of Radiation Damage in Carbon Nanotube Field-Effect Transistors,” *IEEE Transactions on Nuclear Science*, 60(6):4087-4093 (Dec. 2013).

[4] Hong W., Lee C., Nepal D., Geckeler K., Shin K., and Lee T. “Radiation hardness of the electrical properties of carbon nanotube network field effect transistors under high-energy proton irradiation,” *Nanotechnology*, 17:5675-5680 (2006).

[5] Cress C. D., McMorrow J. J., Robinson J. T., Friedman A. L., and Landi B. J. “Radiation Effects in Single-Walled Carbon Nanotube Thin-Film-Transistors,” *IEEE Transactions on Nuclear Science*, 57(6):3040-3045 (2010).

[6] Rossi J. E., Cress C. D., Helenic A. R., Schauerman C. M., DiLeo R. A., Cox N. D., Messenger S. R., Weaver B. D., Hubbard S. M., and Landi B. J. “Ion irradiation of electronic-type-separated single wall carbon nanotubes: A model for radiation effects in nanostructured carbon,” *Journal of Applied Physics*, 112, 034314 (2012).

[7] Walker D., Mann C. J., Nocerino J. C., Liu S. H. “Proton Irradiation of Metallic Single-Walled Carbon Nanotubes,” *Photovoltaic Specialists Conference*, 37:001630-001633 (June 2011).

[8] Cress C. D., Schauerman C. M., Landi B. J., Messanger S. R., Raffaelle R. P., and Walters R. J. “Radiation effects in single-walled carbon nanotube papers,” *Journal of Applied Physics*, 107, 014316 (2010).

[9] Rius G., Martin I., Godignon P., Bachtold A., Bausells J., Lora-Tamayo E., and Perez-Murano F. “Response of carbon nanotube transistors to electron beam exposure,” *Microelectronic Engineering*, 84:1596-1600 (2007).

[10] Best, J. S. (2013) “Electron Damage Effects on Carbon Nanotube Thin Films,” MS Thesis, AFIT/GNE/ENP/13M-37. Graduate School of Engineering &

Management, Air Force Institute of Technology (AU), Wright Patterson AFB OH, March 2013 (ADA583055).

[11] Stassinopoulos E. G. and Raymond J. P. "The Space Radiation Environment for Electronics," *Proceedings of the IEEE*, 76(11):1423-1442 (Nov 1988).

[12] Holmes-Siedle, A. and Adams, L. *Handbook of Radiation Effects* (2nd Edition). Oxford: Oxford University Press, 2002.

[13] Jaeger R. C. and Blalock T. N. *Microelectronic Circuit Design* (4th Edition). New York: McGraw-Hill, 2011.

[14] Petrosky J. Class handout, NENG 660, Radiation Effects on Electronics. Graduate School of Engineering & Management, Air Force Institute of Technology, Wright-Patterson AFB OH, Summer Quarter 2013.

[15] Groeseneken G., Maes H. E., Beltran N., and Keersmaecker R. F. de, "A Reliable Approach to Charge-Pumping Measurements in MOS Transistors," IEEE Transactions on Electron Devices, ED-31(1):42-53 (Jan 1984).

[16] Diaz R., Grisolia J., BenAssayag G., Schamm-Chardon S., Castro C., Pecassou B., Dimitrakis P., and Normand P., "Extraction of the characteristics of Si nanocrystals by the charge pumping technique," Nanotechnology, 23:085206 (2012).

[17] Bosch G. V. den, Groeseneken G. V., Heremans P., and Maes H. E. "Spectroscopic charge pumping: A new procedure for measuring interface trap distributions on MOS transistors," *IEEE Transactions on Electron Devices*, 38(8):1820–1831 (1991).

[18] Marulanda J. M. and Srivastava A. "Carrier density and effective mass calculations in carbon nanotubes," *Phys. Stat. Sol. B*, 245:2558–2562 (2009).

[19] Dresselhaus M. S., Dresselhaus G., and Eklund P. C., *Science of Fullerenes and Carbon Nanotubes*. New York, NY, USA: Academic, (1996).

[20] Grove A. S., *Physics and Technology of Semiconductor Devices*. New York, NY, USA: Wiley, 1967.

[21] Dresselhaus M. S., Dresselhaus G., and Saito R. "Physics of Carbon Nanotubes," *Carbon*, 33(7):883-891 (1995).

[22] Iijima S. S. “Single-shell carbon nanotubes of 1-nm diameter," *Nature* (London), 363(6430):603-605 (1993).

[23] Iijima S. “Growth of carbon nanotubes," Materials science and engineering, 19(1-2):172 (1993).

[24] Iijima S. S. “Carbon nanotubes: past, present, and future," *Physica B: Condensed Matter*, 323(104):1-5 (2002).

[25] Durkop T., Kim B. M. and Fuhrer M. S. “Properties and applications of high-mobility semiconducting nanotubes,” *Journal of Physics: Condensed Matter*, 16:R553-R580 (2004).

[26] Stetter J. R. and Maclay G. J. “Carbon Nanotubes and Sensors: a Review,” *Advanced Micro and Nanosystems*, 1:357-382 (2004).

[27] Arnold M. S., Green A. A., Hulvat J. F., Stupp S. I., and Hersam M. C. “Sorting carbon nanotubes by electronic structure using density differentiation,” *Nature Nanotechnology*, 1:60-65 (Oct. 2006).

[28] Yanagi K., Udoguchi H., Sagitani S., Oshima Y., Takenobu T., Kataura H., Ishida T., Matsuda K., and Maniwa Y. “Transport Mechanism in Metallic and Semiconducting Single-Wall Carbon Nanotube Networks,” *ACS Nano*, 4(7):4027-4032 (2010).

[29] Bandaru P. R. “Electrical Properties and Applications of Carbon Nanotube Structures,” *Journal of Nanoscience and Nanotechnology*, 7:1-29 (2007).

[30] Avouris P., Appenzeller J., Martel R., and Wind S. J. “Carbon Nanotube Electronics,” *Proceedings of the IEEE*, 91(11):1772-1784 (Nov 2003).

[31] Dresselhaus M., Dresselhaus G., Saito R., and Jorio A. “Raman spectroscopy of carbon nanotubes,” *Physics Reports*, 409(2):47-99 (Mar. 2005).

[32] Thomsen C. and Reich S. “Raman Scattering in Carbon Nanotubes,” *Topics in Applied Physics*, 108:115-232 (2007).

[33] Dresselhaus M. S., Saito R., and Jorio A. “Semiconducting Carbon Nanotubes,” Unpublished.

[34] Biercuk M. J., Ilani S., Marcus C. M., and McEuen P. L. “Electrical Transport in Single-Wall Carbon Nanotubes,” *Topics in Applied Physics*, 111:455-493 (2008).

[35] Corio P., Santos P. S., Pimenta M. A., and Dresselhaus M. S. "Evolution of the molecular structure of metallic and semiconducting carbon nanotubes under laser irradiation," *Chemical Physics Letters*, 360:557-564 (2002).

[36] Kracheninnikov A. V. and Norlund K. "Irradiation effects in carbon nanotubes," *Nuclear Instrumentation and Methods in Physics Research B*, 216:355-366 (2004).

[37] Chen Z., Appenzeller J., Knoch J., Lin Y.-M., and Avouris P. "The Role of Metal-Nanotube Contact in the Performance of Carbon Nanotube Field-Effect Transistors," *Nano Letters*, 5(7):1497-1502 (2005).

[38] RamBabu B., Swapna P., Kalyan B. K., and Rao Y. S. "Carbon Nanotubes Field Effect Transistors: A Review," *Internation Journal of Electronics & Commnication Technology*, 2:204-208 (Dec. 2011).

[39] Kang D., Park N., Hyun J., Bae E., Ko J., Kim J., and Park W. "Adsorption-induced conversion of the carbon nanotube field-effect transistors from ambipolar to unipolar behavior," *Applied Physics Letters*, 86, 093105 (2005).

[40] Hong G., Zhang B., Peng B., Zhang J., Choi W. M., Choi J.-Y., Kim J. M and Liu Z. "Direct Growth of Semiconducting Single-Walled Carbon Nanotube Array," *Journal of the American Chemical Society Communications*, 131:14642-14643 (2009).

[41] Javey A., Kim H., Brink M., Wang Q., Ural A., Guo J., Mcintyre P., Mceuen P., Lundstrom M., and Dai H. "High-κ dielectrics for advanced carbon-nanotube transistors and logic gates," *Nature Materials*, 1:241-246 (Dec. 2002).

[42] Islam A. E., Du F., Ho X., Jin S. H., Dunham S., and Rogers J. A. "Effects of variations in diameter and density on the statistics of aligned array carbon-nanotube field effect transistors," *Journal of Applied Physics*, 111:054511 (2012).

[43] Ong H. G., Cheah J. W., Zho X, Li B., Cao X. H., Tantang H., Li L.-J., Zhang H., Han G. C., and Wang J. "Origin of hysteresis in the transfer characteristics of carbon nanotube field effect transistor," *Journal of Applied Physics D: Applied Physics*, 44:285301 (2011).

[44] Kim W., Javey A., Vermesh O., Wang Q., Li Y., and Dai H. "Hysteresis Caused by Water Molecules in Carbon Nanotube Field-Effect Transistors," *Nano Letters*, 3(2):193-198 (2003).

[45] Pascal-Levy Y., Shifman E., Pal-Chowdhury M., Kalifa I., Rabkin T., Shtempluck O., Razin A., Kochetkov V., and Yaishi Y. E. "Water-assisted mobile charge induced screening and origin of hysteresis in carbon nanotube field-effect transistors," *Physical Review B*, 86:115444 (2012).

[46] Jin S. H., Islam A. E., Kim T., Kim J., Alam M. A., and Rogers J. A. "Sources of Hysteresis in Carbon Nanotube Field-Effect Transistors and Their Elimination Via Methylsiloxane Encapsulants and Optimized Growth Procedures," *Advanced Functional Material*, 22:2276-2284 (2012).

[47] Franklin A. D., Tulevski G. S., Han S.-J., Shahrjerdi D., Cao Q., Chen H.-Y., Wong H.-S. P., and Haensch W. "Variability in Carbon Nanotube Transistors: Improving Device-to-Device Consistency," *ACS Nano*, 6(2):1109-1115 (2012).

[48] Banhart F. "Irradiation effects in carbon nanostructures," *Rep. Prog. Phys.*, 62:1181-1221 (1999).

[49] Srour J. R., Marshall C. J., Marshall P. W. "Review of Displacement Damage Effects in Silicon Devices," *IEEE Transactions on Nuclear Science*, 50(3):653-670 (June 2003).

[50] Schwank J. R., Shaneyfelt M. R., Fleetwood D. M., Felix J. A., Dodd P. E., Paillet P., Ferlet-Cavrois V. "Radiation Effects in MOS Oxides," *IEEE Transactions on Nuclear Science*, 55(4):1833-1853 (Aug 2008).

[51] Kramberger G., Cindro V., Mandic I., Mikuz M., Zavrtanik M. "Effective trapping time of electrons and holes in different silicon materials irradiated with neutrons, protons and pions," *Nuclear Instruments and Methods in Physics Research A*, 481:297-305 (2002).

[52] Basiuk V. and Basiuk E. *Chemistry of Carbon Nanotubes*. American Scientific Publishers, 2008.

[53] Walker D., Mann C. J., Nocerino J. C., and Liu S. H. "Proton irradiation of metallic single-walled carbon nanotubes," *Photovoltaic Specialists Conference, 2011 37th IEEE*, 01630-01633 (June 2011).

[54] Neupane P. P., Manasreh M. O., Weaver B. D., Rafaelle R. P., and Landi B. J. "Proton irradiation effect on single-wall carbon nanotubes in a poly(3-octylthiophene) matrix," *Applied Physics Letters*, 86:221908 (2005).

[55] Hong W.-K., Lee C., Nepal D., Geckeler K. E., Shin K. and Lee T. “Radiaition hardness of the electrical properties of carbon nanotube network field effect transistors under high energy proton irradiation,” *Nanotechnology*, 17:5675-5680 (2006).

[56] Buchowicz G., Stone P. R., Robinson J. T., Cress C. D., Beeman J. W., Dubon O. D. “Correlation between structure and electrical transport in ion-irradiated graphene grown on Cu foils,” *Applied Physics Letters*, 98:032102 (2011).

[57] Hulman M., Skakalova V., Roth S., Kuzmany H. “Raman spectroscopy of single-wall carbon nanotubes and graphite irradiated by gamma rays,” *Journal of Applied Physics*, 98:024311 (2005).

[58] Wu Z., Chen Z., Du X., Logan J. M., Sippel J., Nikolou M., Kamaras K., Reynolds J. R., Tanner, D. B., Hebard A. F., and Rinzler A. G. “Transparent, Conductive Carbon Nanotube Films,” Science, 305(5688):1273-1276 (Aug 2004).

REPORT DOCUMENTATION PAGE

Form Approved
OMB No. 0704-0188

1. REPORT DATE (DD-MM-YYYY)	2. REPORT TYPE	3. DATES COVERED (From - To)
19-06-2014	Master's Thesis	OCT 2012 - JUN 2014

4. TITLE AND SUBTITLE

Proton Damage Effects on Carbon Nanotube Field-Effect Transistors

5a. CONTRACT NUMBER

5b. GRANT NUMBER

5c. PROGRAM ELEMENT NUMBER

6. AUTHOR(S)

Kemp, Evan R., Mr.

5d. PROJECT NUMBER

14P168

5e. TASK NUMBER

5f. WORK UNIT NUMBER

7. PERFORMING ORGANIZATION NAME(S) AND ADDRESS(ES)
Air Force Institute of Technology
Graduate School of Engineering and Management (AFIT/EN)
2950 Hobson Way
Wright-Patterson AFB OH 45433-7765

8. PERFORMING ORGANIZATION REPORT NUMBER

AFIT-ENP-T-14-J-39

9. SPONSORING/MONITORING AGENCY NAME(S) AND ADDRESS(ES)

POC: MAJ Thomas McQuary (thomas.mcquary@dtra.mil)

Defense Threat Reduction Agency
8725 John J. Kingman Rd
Ft. Belvoir, VA 22060

10. SPONSOR/MONITOR'S ACRONYM(S)

DTRA

11. SPONSOR/MONITOR'S REPORT NUMBER(S)

12. DISTRIBUTION/AVAILABILITY STATEMENT

DISTRIBUTION STATEMENT A. Approved for public release; distribution is unlimited.

13. SUPPLEMENTARY NOTES

This material is declared a work of the U.S. Government and is not subject to copyright protection in the United States.

14. ABSTRACT

This research investigated the effects of proton damage on single-walled carbon nanotube (SWCNT) transistors. The transistors were irradiated by 1.8 MeV protons to determine the damage induced in the SWCNTs and the device substrate using Raman spectroscopy, and to observe the effect on transistor functionality by measuring current-voltage characteristics. Irradiation of the SWCNT transistors to a fluence of 1×10^{13} protons/cm^2 resulted in 67% increase in the Raman *D/G* peak intensity ratio, while at a fluence of 2×10^{13} protons/cm^2 the increase in the *D/G* ratio was only 18%, likely due to radiation annealing. Current-voltage measurements indicated an increasingly negative threshold voltage shift in SWCNT transistors as a function of proton fluence: -1.3 V after a fluence of 1×10^{12} protons/cm^{2}and -1.9 V after a fluence of 2×10^{13} protons/cm^2. The drain current decreased 33% after a fluence of 1×10^{12} protons/cm^2 and 58% after a fluence of 2×10^{13} protons/cm^2. Charge pumping of the SWCNT transistors revealed a significant error attributed to the combination of the non-uniform distribution of SWCNTs across the gate region, adsorbates on the exposed SWCNT and gate oxide surfaces, and inconsistency in transistor performance. The transistor hysteresis also increased as a function of the proton fluence due to interface and bulk charge trapping. This research provided insight into the effect on SWCNT transistors due to proton irradiations up to a fluence of 2×10^{13} protons/cm^2 demonstrating both interface and bulk damage effects.

15. SUBJECT TERMS

carbon nanotube, field-effect transistors, radiation effects

16. SECURITY CLASSIFICATION OF:			17. LIMITATION OF ABSTRACT	18. NUMBER OF PAGES	19a. NAME OF RESPONSIBLE PERSON
a. REPORT	b. ABSTRACT	c. THIS PAGE			Dr. John McClory AFIT/ENP
U	U	U	UU	96	19b. TELEPHONE NUMBER (Include area code) (937) 255-3636 x 7308 john.mcclory@us.af.mil